Chlorine-assisted synthesis of Mn-deficient $LiMn_2O_4$ spinel with ultra-high-rate capability and long-term cyclability in half and full Li ion cells

View Article Online
DOI: 10.1039/D3TA06646K

F. Luna-Lama[1], L. Barbosa[2], A.Y. Tesio[1,3], A. Caballero[1], J. Morales[1*]

[1]Departamento de Química Inorgánica e Ingeniería Química, Instituto Químico de la Energía y el Medioambiente (IQUEMA), Universidad de Córdoba, 14014, Córdoba, Spain.

[2]Instituto de Investigación en Tecnología Química (CONICET), Facultad de Química Bioquímica y Farmacia (UNSL), Almirante Brown 1455, San Luis (D5700HGC), Argentina.

[3]Centro de Investigación y Desarrollo en Materiales Avanzados y Almacenamiento de Energía de Jujuy (CIDMEJu), Centro de Desarrollo Tecnológico General Manuel Savio, Palpalá, Jujuy, 4612, Argentina.

[*]Corresponding Author: iq1mopaj@uco.es; Tel.: +34–957218620

Abstract

A different route is proposed to reduce the Mn^{3+} content in $LiMn_2O_4$ spinel. Manganese ions are responsible for both the Jahn-Teller distortion and the dissolution of Mn in the electrolyte, the main causes of low cycling stability and limited rate capability. For this, Cl_2 was used as an oxidising agent to promote partial oxidation of Mn^{3+} without destroying the spinel structure. The X-ray diffraction (XRD) pattern recorded with $Mo_{k\alpha 1}$ confirmed the formation of a spinel defective in Mn, with $Li_{1.06}Mn_{1.94}O_4$ stoichiometry. The Mn vacancies were occupied by excess Li together with the presence of a layered Li_2MnO_3 phase as an impurity. Combining SEM images and EDX spectra, it was possible to differentiate both components as independent phases with different morphology. The spinel has a remarkable rate capability in the half-cell configuration from 1C to 50C, delivering an average capacity of 130 to 96 mAh g^{-1}, respectively. Also, it has excellent cycling stability, as revealed by the capacity retention values, between 98–96% from 0.5 (500 cycles) to 10C (1000

View Article Online
DOI: 10.1039/D3TA06646K

cycles), maintaining high capacity values, from 138 to 127 mAh g^{-1}, respectively. Furthermore, it can deliver high power, 26196 W kg^{-1}, with a high energy of 322 Wh kg^{-1}. To our knowledge, our spinel delivers the highest specific energy for lower power values reported so far. These excellent properties can be attributed to both its Mn deficiency, which decreases Mn^{3+}, and the good transport properties obtained from CV and EIS techniques. The first, together with the high crystallinity and micrometric particle size, would mitigate the dissolution of Mn and enhance the structure stability. On the other hand, the high rates that the electrode supports can be ascribed to the high values of Li^+ diffusion coefficient averaged to the different stages of the process, around 4 x 10^{-10} cm^2 s^{-1}. Spinel also provides satisfactory performance in full cells using MCMB as an anode and a positive/negative ratio close to 1 without the need for a prelithiation process. Thus, for power values of 10567 W kg^{-1}, it supplied an energy of 196 Wh kg^{-1}.

Keywords: lithium-ion batteries; LMO spinel; spodumene; chlorine; full-cells

1. Introduction

Currently, rechargeable Li-ion batteries (LIB) are the only electrochemical storage energy systems capable of meeting the energy needs of numerous electronic devices as well as the incipient implementation of electric vehicles (EVs). Extensive attention has been paid to developing cathode materials. Two of these are based on different frameworks of oxide ions, and the ones that have had the most success are $LiCoO_2$ and $LiMn_2O_4$. Hence, there is abundant literature available on these.[1–7] Although the capacities they provide are similar, LMO provides a higher voltage (4.0 V) than $LiCoO_2$ (3.6 V). Moreover, the lower toxicity and greater abundance of Mn compared to Co is another advantage of the compound. The main drawback is the capacity drop observed on prolonged cycling. This is due to different causes, mainly associated with the structural stability of the spinel framework[8] and Mn dissolution in the electrolyte.[9,10] The Jahn-Teller effect of Mn^{3+} is the origin of the structural instability of the spinel. The distortion of individual Mn^{3+} can be observed by the lattice parameter

View Article Online
DOI: 10.1039/D3TA06646K

change using by the differential functional theory (DFT) through the GGA+U model.[11] This effect leads to a splitting of the Mn^{3+} O bond length and a change in the structure from cubic to tetragonal observed at temperature below 100 K.[12] The suppression of Jahn–Teller distortion by Cr and Mg doping in this spinel has also been studied by DFT.[13] However, the GGA model predicts Cr to be more effective than Mg in suppressing the JT distortion while GGA+U model predicts Mg to be more effective. These divergences have also been found in other electronic properties of the $LiMn_2O_4$ spinel itself, since the GGA model predicts a metallic behavior while GGA+U predicts to be insulating, closer to the experimental observations. The Mn^{3+} ion is also unstable to disproportionation ($Mn^{3+} \rightarrow Mn^{4+} + Mn^{2+}$), especially favourable in acid medium, conditions that would create HF and whose origin is feasible due to the electrolyte salt, $LiPF_6$. This is the model used to explain the second origin of spinel instability, Mn dissolution in the electrolyte. Both issues are the main factors responsible for the capacity fading over extended cycles.

Several strategies have been implemented to overcome these drawbacks. Surface coating has been suggested as the most direct and effective means of reducing Mn dissolution,[14] giving special relevance to carbon due to its conductive properties.[15–17] To mitigate the Jahn-Teller distortion, the most common method has been partial substitution of Mn^{3+} by different aliovalent ions of Fe, Al, and Cr, among others.[18–21] Even other valences, such as Mg^{2+}, in this case using $MgCl_2$ as the source of the element, have been tested. In this case, Cl^- ions have been suggested as co-doping ions to maintain electroneutrality in the spinel composition.[22] Reducing the particle size to the nanoscale is another alternative that has received great attention. This aims to shorten the diffusion distances of Li^+ to enhance Li migration, resulting in better high-rate performance.[4,23,24] However, both proposals can cause adverse results by reducing the total cell capacity due to the inactive electrochemical behaviour of the dopant cations[25,26] and the poor packing density of nanoparticles.[27] Moreover, the increased reactivity of nanoparticles may enhance Mn dissolution in the electrolyte.

Here, we adopt a different approach to minimising the Jahn-Teller effect in parallel to decreasing Mn^{3+} in the spinel. Our approach uses a strong oxidising agent such as Cl_2 to induce partial oxidation

View Article Online
DOI: 10.1039/D3TA06646K

of Mn^{3+} to Mn^{4+}, maintaining the spinel structure. The synthesised spinel is highly crystalline with a small excess of Li and a deficiency of Mn, $Li_{1.06}Mn_{1.94}O_4$, and a small content of the layered phase Li_2MnO_3, which does not affect the electrochemical reactions of the spinel in the potential window selected (4.5 –3.0 V). This synthesis method can give rise to different intrinsic point defects in addition to the Mn and Li antisites that can improve the diffusion properties of Li ions as suggested by the results of the DFT calculations.[28–30] In addition, LiCl obtained from β-spodumene (β-$LiAlSi_2O_6$) was used as a Li source. This is the most common and most studied Li mineral.[31] The mineral was roasted with $CaCl_2$ as the chlorination agent, with the subsequent formation of LiCl. This strategy is different from the one usually used as a synthesis method which consists of using commercial Li compounds (mainly as hydroxide or oxysalts).

2. Experimental Section

2.1 Spinel synthesis.

The synthesis of the lithium manganese spinel was performed by a solid-state reaction. The manganese source was analytical grade $MnCO_3$ (Carlo Erba). According to our previous study, the lithium source was LiCl obtained from β-spodumene by chlorination from roasting.[32] The solid reagents were mixed in an agate mortar using a 10% (w/w) excess of LiCl to balance the losses of volatile LiCl. This mixture was put into an evaporation-type capsule by distributing the powder in a thin layer over the capsule. Then, the mixture was calcined in a muffle furnace at 700 °C for 11 h. Subsequently, this sample was heat treated in a Cl_2/N_2 atmosphere in a quartz T-type reactor equipped with an electric furnace and designed to function in corrosive and non-corrosive atmospheres. The sample was put in a quartz sample holder and placed in the centre of the reactor. Then, the heating started at a 5 °C min^{-1} rate. When it reached 400 °C, a 100 mL min^{-1} flow of Cl_2/N_2 (10/90, v/v) was immediately introduced into the reactor. The sample was kept at 400 °C in a Cl_2/N_2 atmosphere for 2 h. After this period, the roasted chlorination sample was withdrawn from the reactor and cooled. After

View Article Online
DOI: 10.1039/D3TA06646K

the cooling period, the sample was washed with distilled water at 70 °C for 0.5 h with continuous stirring. The suspension was filtered to separate the solid particles. Finally, the wet solid was dried in an oven to give a sample labelled LMO-Cl. The scheme of the synthesis method and cell assembly are shown in Fig. 1. A commercial spinel (Sigma-Aldrich), labelled LMO-C, was used for comparative characterisation purposes.

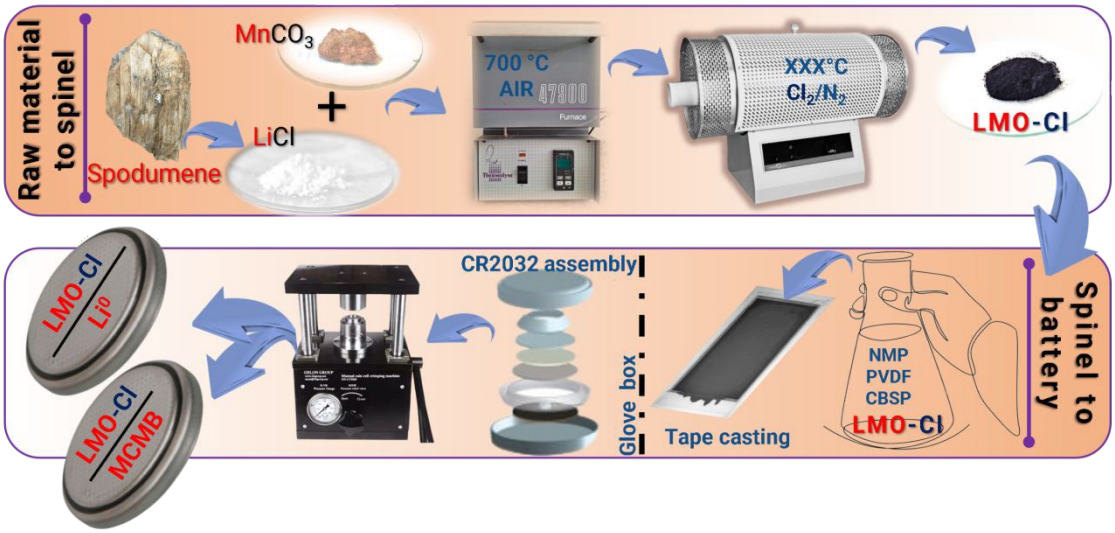

Figure 1. Synthetic procedure for LMO-Cl and assembly of the cell types studied: LMO-Cl/Li and LMO-Cl/MCMB.

2.2 Characterization methods.

The phase composition and crystal structure were determined from powder X-ray diffraction (XRD) with a Bruker D8 Advance diffractometer equipped with $CuK_{\alpha 1}$ and $MoK_{\alpha 1}$ monochromatic radiation (λ = 1.5406 and 0.7093 Å, respectively). The shorter wavelength of Mo gives a significant improvement over Cu, i.e., a large Q range and a larger penetration depth. For this reason, the XRD pattern of Mo was used for the structure refinement. Transmission powder X-ray diffraction data using $MoK_{\alpha 1}$ radiation were recorded at the Centralized Research Support Services (SCAI) of the University of Malaga using a Bruker D8 ADVANCE diffractometer. The incident beam consists of a primary monochromator + focussing mirror and a 2 mm anti-scatter slit, and a 2.5 º soller was used in both the incident and transmitted beams. The detection system consists of an EIGER detector (from the commercial company DECTRIS) specially designed and optimised for Mo anodes. The detector

View Article Online
DOI: 10.1039/D3TA06646K

was used with an aperture of 4 x 21 degrees. Measurements were made from 5 to 60 º (2θ) for 3.5 h. The tube worked at 50 kV and 50 mA. Raman spectra were measured with a confocal Raman spectrometer alpha500 (WITec) with a frequency doubled Nd:YAG laser (532 nm). The laser beam was focused on the sample using a 20x/0.4 Zeiss objective, and the Raman spectra were recorded with an integration time of 1 s by accumulating a total of 10 spectra. SEM images of the materials were obtained with a JSM–7800 (JEOL) scanning electron microscope equipped with an X–ACT (Cambridge Instrument) detector for EDS elemental microanalysis. HRTEM images were obtained with Talos F200i (Thermo Fisher Scientific) microscope with STEM-HAADF transmission scanning imaging system, X-ray energy dispersive microanalysis system, EDX and digital camera. The Brunauer–Emmett–Teller (BET) specific surface area was obtained from N_2 adsorption–desorption isotherms at liquid nitrogen temperature (77 K) with an ASAP 2020 (Micromeritics) using nitrogen gas as an adsorbate. X-ray photoelectron spectroscopy (XPS) spectra were recorded with a PHOBIOS 150 MCD SPECS spectrometer with monochromatic Mg-Kα (1253.6 eV) radiation and a multichannel detector in a chamber able to reach a pressure of 4 x 10^{-9} mbar.

Spectra of the samples were recorded in the constant pass energy mode at 29.35 eV, using a 720 µm diameter analysis area. Binding energy (BE) values were referred to the C 1*s* peak at 284.8 eV. The CA PHI ACCESS ESCA–V6.0 F software package was used for data acquisition and processing. A Shirley-type background was subtracted from all signals. Recorded spectra were always fitted using Gauss-Lorentz curves to more accurately determine the binding energy of the different element core levels. The cycled electrodes were collected after disassembling the cells inside the glovebox. All samples were soaked in DMC to remove soluble species and then dried inside the glovebox under vacuum; the dried samples were collected in an Eppendorf vessel and sealed for transfer to the XPS instrument. The error in BE was estimated to be ca. ± 0.1 eV.

2.3 Electrode preparation and cell assembly.

The active material, LMO or MCMB–6–28 (mesocarbon microbeads supplied by Osaka Gas), was mixed in a mortar with carbon black and PVDF in a ratio 80:10:10 by weight. Approximately 9 mL

View Article Online
DOI: 10.1039/D3TA06646K

of NMP was added dropwise to the mixture, and the slurry formed was maintained under stirring for 24 h at 300 rpm. The doctor blade technique was used to spread the slurry over a substrate of carbon cloth (ELAT LT 1400, FuelCellStore). The choice of carbon cloth is based on the improvement in capacity obtained by Di Lecce et al.[33] with this substrate compared to that of Al foil in Li cells with olivine cathodes, around 9%. Cu foil of 9 μm was used as the anode substrate. Slurry-coated foils were dried in an oven overnight at 50 °C. The dried deposits were punched with a manual punching machine into 13 mm diameter discs with the same loading for LMO and MCMB, 1.5 mg cm^{-2}. The discs were additionally dried in a glass oven (Büchi) under vacuum for 3 h. The two-electrode coin cells, CR2032 model, were assembled in a dry argon-filled glove box (M. Braun; $H_2O \leq 1$ ppm). $LiPF_6$ (1M) dissolved in EC and DEC (1:1) was used as the electrolyte, and a 16 mm diameter fibreglass disc (Whatman) was used as the separator. Electrochemical cycling tests were performed on a battery tester system (Arbin BT2143, Arbin Instruments) in a voltage range of 3.0–4.5 V. Galvanostatic discharge–charge tests were carried out under constant current rates of 0.5C, 1C, 5C, 10C, 50C and 100C (1C = 148 mA g^{-1}). Rate capability tests were performed under current rates of 0.1C, 0.2C, 0.5C, 1C, 2C, 5C, 10C, 20C, 50C and 100C, increasing every 5 cycles and then returning to 0.1C for 20 cycles. The cyclic voltammetry (CV) and electrochemical impedance spectroscopy (EIS) measurements were recorded together at the open circuit voltage (OCV) stage after several discharge–charge cycles with a potentiostat Pgstat204 (Metrohm Autolab). The CV measurements were performed with a scan rate of 0.1 mV s^{-1} in a voltage range of 3.0–4.5 V. The EIS measurements were recorded in a frequency range from 0.1 Hz to 500 kHz with a disturbance amplitude of 10 mV. The CV measurements for the Randles–Sevick calculations were also carried out in the same potentiostat under different scan rates of 0.1, 0.2, 0.3, 0.5, 0.8, and 1 mV s^{-1} using the same voltage range. The EIS measurements for D_{Li} calculations were recorded over the same frequency range within different electrode states of charge (SOC) obtained by linear sweep voltammetry (LSV) after a first CV activation cycle was recorded over the same potential range and under a constant scan rate of 0.05 mV s^{-1}.

View Article Online
DOI: 10.1039/D3TA06646K

3. Results and Discussion

3.1 Structural properties

The LMO-Cl sample was obtained as a black powder. The preliminary XRD pattern, recorded with Cu $K_{\alpha1}$ radiation and plotted in Fig. S1a, shows the typical peaks of the $LiMn_2O_4$ spinel structure and weak peaks assignable to the presence of Li_2MnO_3 as a secondary phase which is absent in the LMO-C sample. The XRD patterns recorded with shorter wavelength Mo $K_{\alpha1}$ radiation show the presence of the Li_2MnO_3 layer phase more clearly, Fig. S1b. The Rietveld refinement of this pattern was carried out with the TOPAS VI program.[34] A pseudo-Voigt function was chosen to generate the line shape of the diffraction peaks. The following parameters were refined: zero error, background, scale factor, pseudo-Voigt peak profiles corrected for asymmetry parameters, unit-cell parameters, atomic occupation, and isotropic displacement factors. The obtained Rietveld refinement is plotted in Fig. 2, and the main crystallographic results are listed in Table 1.

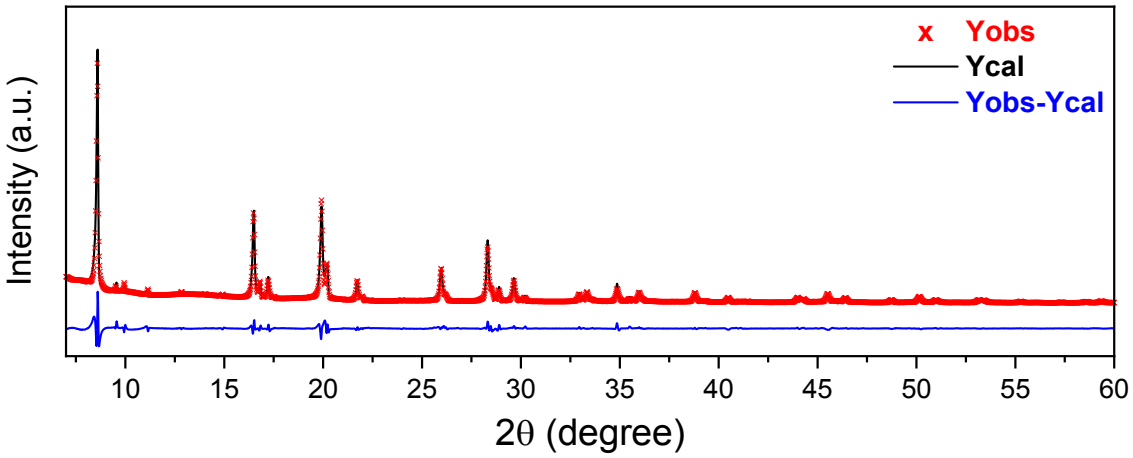

Figure 2. Rietveld refinement of the X-ray Mo$K_{\alpha1}$ pattern for LMO-Cl sample.

Table 1. Crystallographic parameters for $LiMn_2O_4$ (sample LMO-Cl).

Cubic ($Fm\bar{3}m$); a = 8.1993(3) Å and V = 551.23(5) Å^3 wt%=79.5(5)						
Atoms	***Wichoff site***	***x***	***y***	***Z***	U_{iso}	f_{occ}
Li1	8[a]	0.125	0.125	0.125	0.0051(5)	1
Mn2	16*d*	0.5	0.5	0.5	0.0094(5)	0.94

Li2	16*d*	0.5	0.5	0.5	0.0094(5)	0.06
O	32*e*	0.2589(2)	0.2589(2)	0.2589(2)	0.0201(9)	1

View Article Online
DOI: 10.1039/D3TA06646K

Reliability Factors: R_p = 3.35%, R_{wp} = 4.81%, GOF=4.18,

The secondary phase, lithium trioxo-manganate is refined with the data of bibliography, only the lattice parameters, scale factors and scale factor are refined, giving a value of wt% of 20.5(5)

The spinel was correctly modelled using the spinel cubic symmetry model (SG: $Fd\bar{3}m$). In this structure, the Li^+ and $Mn^{3+/4+}$ cations are in 8*a* and 16*d* Wyckoff sites, respectively. The lithium and manganese atoms are close packed by oxygen atoms at the 32*e* site in the tetrahedral and octahedral forms, respectively. The diffraction data were well fitted to a spinel with a small excess of Li, which substitutes for Mn in the 16*d* site with a nominal composition of $Li_{1.06}Mn_{1.94}O_4$. The average Mn oxidation state should be 3.57, with a small excess of Mn^{4+} (Mn^{4+}/Mn^{3+} atomic ratio = 1.12/0.82). These results are consistent with the oxidising properties of Cl_2, which partially oxidises Mn^{3+} to Mn^{4+}. Also, the smaller ionic radius of Mn^{4+} (67 pm) compared with that of Mn^{3+} (78.5 pm), along with the occupation of a small fraction of *16d* positions by Li^+ (ionic radius 90 pm),[35] could explain the reduction of the unit cell volume, Table 1, compared with that of the spinel $LiMn_2O_4$.[36] Usually, the unit cell parameter commonly informed for $LiMn_2O_4$ spinel is around 8.24 Å. However, in our case, its value is less than 8.20 Å. This decrease could also be related to changes in the Li/Mn ratio. Different reports describe similar behaviour in $Li_{1+x}Mn_{2-x}O_4$ spinels, with a tendency for unit-cell reduction as x increases.[37,38] Furthermore, this decrease in unit cell volume does not support the substitution of O^{2-} by Cl^-, with ionic radii 140 and 167 pm, respectively, as reported in chlorine-doped spinels.[22,39] The Li_2MnO_3 phase was refined in the monoclinic system (SG *C/2m*) based on the structure reported by Strobel and Lambert-Andron,[40] and its content was around 20 (5)% w/w. The formation of the layered Li_2MnO_3 phase in the preparation of the $LiMn_2O_4$ spinel has also been detected when the synthesis is carried out at higher temperatures (above 800 ºC). This is caused by the loss of Li through volatilisation.[38] The presence of Ni^{2+} facilitates the formation of the layered

View Article Online
DOI: 10.1039/D3TA06646K

Li–Mn phase at lower temperatures, together with a second layered $LiNi_{0.5}Mn_{0.5}O_2$ phase with a rhombohedral structure (*R3m*).[41]

The SEM of the LMO-Cl sample is shown in Fig. 3a. The octahedral shape is the predominant morphology of the particles, revealing that the spinel is highly crystalline. Particle sizes range from 0.5–1 μm. There are also some smaller particles with irregular shapes that we tentatively associate with the Li_2MnO_3 phase based on the EDX data. As an example, Fig. S2a shows the SEM image used to record the EDX spectra in the area marked by two circles s. 40 (spinel particle) and s. 38 (assigned to Li_2MnO_3 particles) localised in particles of different morphology and size. Their EDX spectra are shown in Figs. S2b and c, respectively. The atomic percentage of O and Mn is shown in Table 2. The average values of the O/Mn ratio of several similar measurements recorded in other octahedral particles were around 2.02, in good agreement with that of the spinel. The same type of measurement was performed for the smaller particles with irregular morphology. In these particles, the O/Mn ratio was around 3.01, a value closer to the layered phase. These results support that both phases are independent and not an intergrowth system. The EDX mapping of the elements was also recorded using STEM images, Fig. S2d. The only elements identified were O and Mn and, as expected, they were homogeneously distributed. Using this technique, the presence of Cl was not detected.

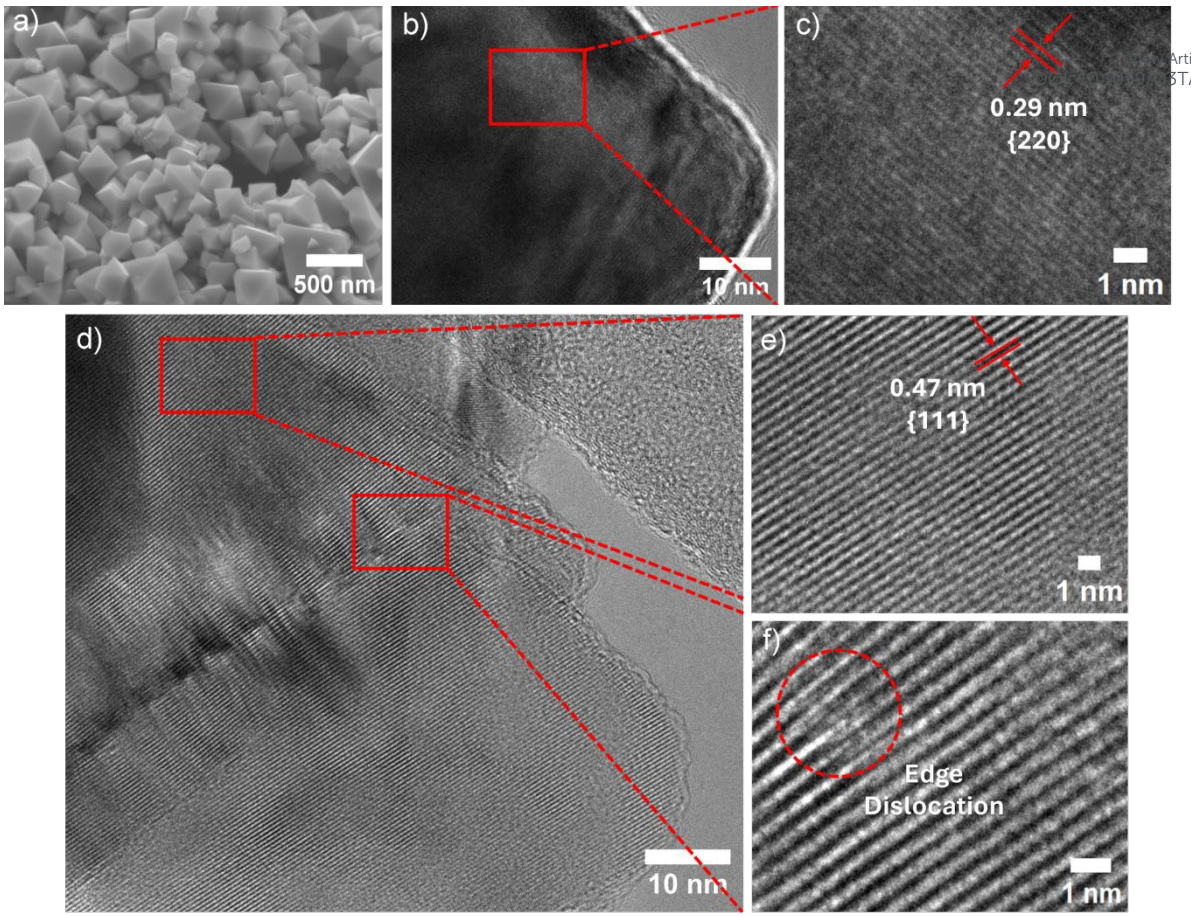

Figure 3. SEM and TEM characterization of LMO-Cl sample. (a) SEM images at different magnification. (b), (c) HRTEM image of the end of one of the triangular faces of an octahedral particle. Lattice distances, 0.29 nm, are consistent with {220} planes. (d) HRTEM image of a particle with lattice fringes with spacings of 0.47 nm assignable to {111} planes. Ordered, (e), and disordered, (f), areas can be observed.

Table 2. Atomic concentration of O and Mn in the regions marked by circles A and B in Fig. S2.

	Weight (% Atomic)	
Element	**Spectrum 40**	**Spectrum 38**
O	67.56	76.69
Mn	32.44	23.31
Total =	100.00	100.00

The HRTEM images of the crystals show ordered lattice fringes consistent with an acceptable crystallinity of $Li_{1.06}Mn_{1.94}O_4$. In Fig. 3b an image of the end of an octahedral particle is shown with the electron beam almost perpendicular to the triangular face, showing lattice fringes with a spacing

View Article Online
DOI: 10.1039/D3TA06646K

of 0.29 nm, (Fig. 3c), consistent with that of {220} planes.[42] In other particles, lattice fringes with a spacing of 0.47 nm, consistent with the spacing of {111} planes of the cubic spinel, are clearly detected, Fig. 3d,e. However, in some area defects are observed in the ordering layers, in particular extra planes associated with edge dislocations, Fig. 3f, which could justify the distortions of the structure because of its stoichiometric deviation. Edge dislocation has also been observed if the spinel is irradiated with ^{60}Co gamma rays.[43] These dislocations cause important changes in the coordination environments of Mn and Li that can reduce the magnitude of the TJ distortion.

The N_2 adsorption/desorption isotherm of the LMO-Cl sample is shown in Fig. S3. The isotherm shape is typical of non-porous solids, type II in the BDDT classification. The shape of the isotherm, type II, and the negligible hysteresis between both curves and the pore volume, 0.02 $cm^3\ g^{-1}$ within measurement error, are evidence of a non-porous material. The polyhedral morphology of the smooth-faced particles shown by the SEM images agrees with the N_2 adsorption measurements. The calculated specific surface area, S_{BET}, is also very low, 9 $m^2\ g^{-1}$.

The XPS spectra of LMO-Cl and LMO-C samples were also recorded to shed additional light on the surface composition and the chemical environment of the elements. The survey spectra are shown in Fig. S4, in which the two elements, Mn and O, are clearly identified together with adventitious carbon coming from the vacuum system. Traces of Cl, just 1% in atomic concentration, were detected in the spine. Its non-identification in the EDX spectra is due to the differences between both spectroscopic techniques. As is well known, XPS gives information at a surface level while EDX is at a more bulk level. The presence of Cl is associated with impurities not being removed after successive washings and not as a doping agent, ruled out by the unit cell dimension values already mentioned. As for Li, its detection difficulty is related to Mn since the Li *1s* photoemission peak overlaps with Mn *3p,* Fig. S5. Nevertheless, a weak and broad asymmetric peak centred around 54.0 eV reveals its presence as Li^+.[44] There is more difficulty in identifying and evaluating the oxidation states of Mn in both spinels. The two most intense peaks corresponding to spin-orbit splitting of Mn $2p_{3/2}$ and $2p_{1/2}$ in both spinels are similar and very symmetric, Figs. 4 a, b. In the case of the LMO-Cl sample, the Li_2MnO_3 impurity

View Article Online
DOI: 10.1039/D3TA06646K

barely affects it. So, their fitting to several components is controversial. Nevertheless, some authors[45,46] fit the Mn $2p_{3/2}$ peak to at least six components based on a model of the multiplet structure of core 2*p*-vacancies levels for 3*d* transition metal ions, incorporating the spin-orbit interaction but ignoring the crystal fields effects, in other words, the local environment.[47] However, the satellite structure for the Mn 2*p* (and 3*p*) levels is not very pronounced, as observed in our spectra. This would be the origin of why other authors prefer the Mn 3*s* photoemission peak to analyse the Mn oxidation states.[48–51] The Mn 3*s* signal splits into two peaks due to the interaction between the 3*s* electron and the 3*d* electrons (exchange interaction).[52] In other words, the ions have two possible final states: Mn^{3+} $(3s^1 3p^6 3d^3)^5S$ or $(3s^1 3p^6 3d^3)^3S$ and Mn^{4+} $(3s^1 3p^6 3d^4)^6S$ or $(3s^1 3p^6 3d^4)^4S$. This is the origin of the splitting, and it appears very clear in the Mn 3*s* photoemission spectrum. For Mn^{3+}, the split is around 5.4 eV, while for Mn^{4+}, it is about 4.5 eV.[49] The Mn 3*s* spectra of the two spinels are shown in Figs. 4c and 4d, and the doublet has different splitting energies, around 5.04 and 4.85 eV, for the LMO-Cl and LMO-C samples, respectively. These values reflect appreciable differences in the oxidation states of Mn. Considering the linear behaviour of the splitting energies for Mn^{n+} (n = 2, 3, 4) versus the oxidation state,[49] the average oxidation state calculated for the LMO-C spinel is 3.49, virtually corresponding to a stoichiometric spinel. The one calculated for the spinel LMO-Cl is much higher, 3.67. This is consistent with an excess of Li in the spinel and the presence of Li_2MnO_3, the latter phase with virtually all Mn as Mn^{4+}. Considering the stoichiometry of the LMO-Cl spinel, $Li_{1.06}Mn_{1.94}O_4$ (1.12 Mn^{4+} and 0.82 Mn^{3+} atoms), and its composition deduced from XRD data, 79.5 and 20.5% for the spinel and Li_2MnO_4, respectively, it is possible through simple calculations to evaluate the average oxidation state of Mn. The value of these calculations, 3.67, is like that evaluated by the XPS spectra, highlighting the good agreement between both characterisation techniques.

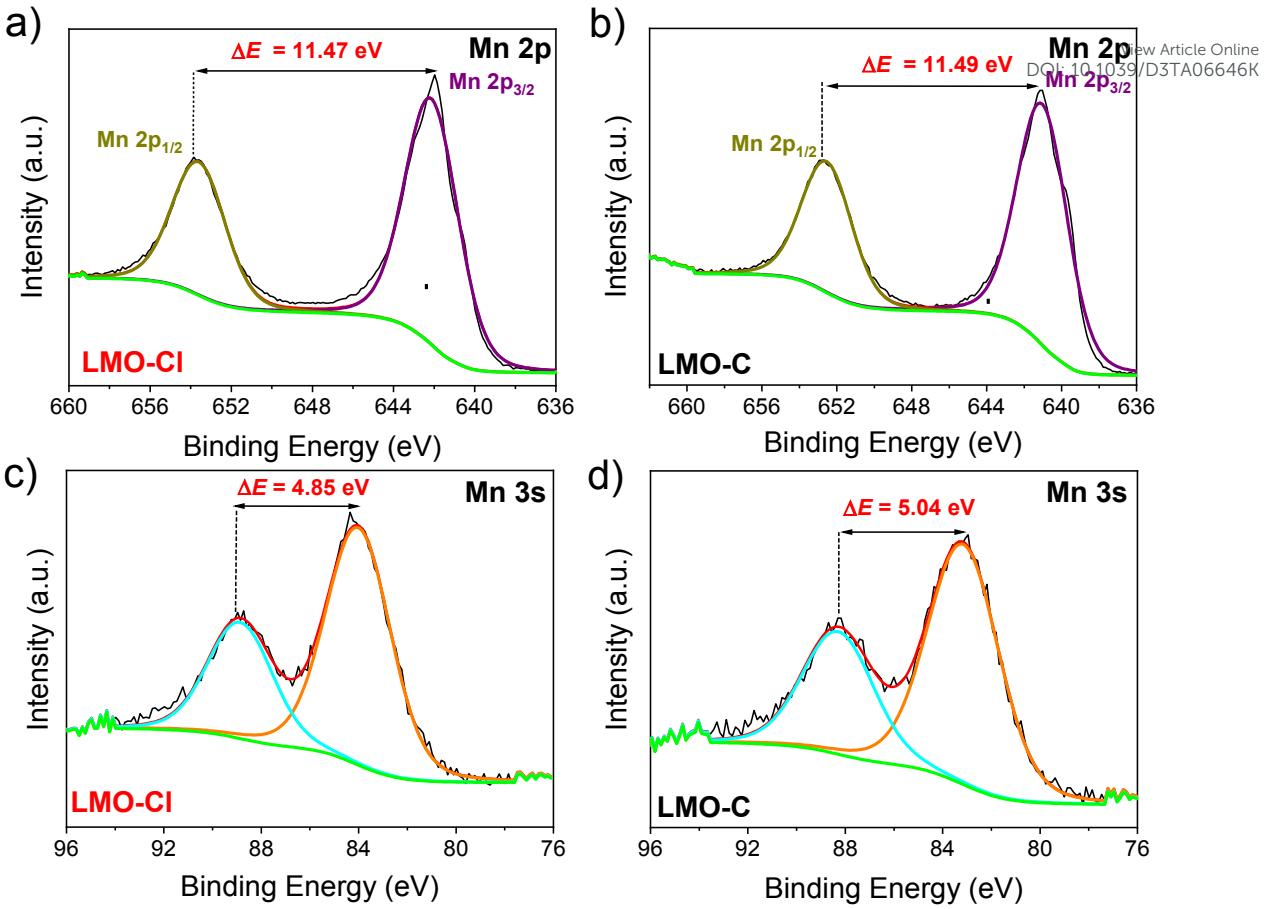

Figure 4. Mn 2*p* (a) and Mn 3*s* (c) photoemission spectra of LMO-Cl sample. The two spectra of LMO-C sample (b, d) are included for comparison.

3.2 Electrochemical properties

3.2.1 Half-cells

The charge/discharge profiles of the LMO-Cl sample for several cycles over the voltage range of 3.0−4.5 V at a rate of 0.1C are shown in Fig. 5a. The shape of both curves hardly changes with cycling and is typical of a Li-Mn spinel, two distinct pseudo-plateaus at around 3.8 and 4.3 V which are assigned to the two reversible Li de-insertion/insertion processes written below according with the spinel composition deduced from ND:

$$Li_{1.06}Mn_{1.94}O_4 \leftrightarrow 0.41\ Li^+ + Li_{0.65}Mn_{1.94}O_4 + 0.41\ e^- \quad (1)$$

$$Li_{0.65}Mn_{1.94}O_4 \leftrightarrow 0.41\ Li^+ + \lambda\text{-}Li_{0.12}Mn_{0.97}O_2 + 0.41\ e^- \quad (2)$$

Regarding the contribution of the Li_2MnO_3 impurity to the electrode capacity, the profile of the charge curve of this compound is very different from the one shown in Fig. 5a since the first charge only

View Article Online
DOI: 10.1039/D3TA06646K

shows an extensive plateau for voltages around 4.5 V, assignable to oxygen release and/or electrolyte oxidation.[53–56] The discharge curve is also different, with a less pronounced voltage drop and without the presence of the two pseudo-plateaus discernible in Fig. 5a.[49] Therefore, the impurity hardly has an effect. Thus, the specific capacity of the electrode must be assigned to the spinel phase. Our results differ from those reported by Johnson et al.[56] on a layered-spinel composite $0.7Li_2MnO_3{-}0.3Li_{1.33}Mn_{1.66}O_4$ structurally integrated. There is no relationship between the initial charge/discharge profiles of this composite calcined at 400 or 750 ºC and that of our LMO-Cl sample. There are several open questions about the origin of this discrepancy, especially about the scant role played by the layered phase in our electrode. First, the characterisation of the composite reported in ref.[56] is limited. It was basically obtained from the Rietveld refinement of XRD patterns recorded by Cu kα radiation, with an insufficient number of reflections for the layered Li_2MnO_3 component, as recognised by the authors themselves. Neither the method of evaluation of the composite composition was indicated nor the evaluation of the spinel non-stoichiometry (we assume that both properties have been deduced from the analysis of the XRD patterns). The two commented properties, the presence of independent particles deduced from the EDX spectra and the shape of the charge/discharge curves typical of spinel, support that both phases in our material are not integrated from a structural point of view. Discharging the cell to 3.0 V delivered a capacity of 140 mAh g^{-1}, close to the theoretical capacity of the electrode, 150 mAh g^{-1}, considering the spinel non-stoichiometry according to equations (1) and (2) and 20% of the impurity which is electrochemically inactive in the potential range used. The shape of the curves hardly changes in subsequent cycling, Fig. 5a, and the electrode shows excellent capacity retention after the 60 cycles tested, Fig. 5b, with a capacity loss of hardly 0.02%. A similar behaviour is observed in the electrode coulombic efficiency, the average value of which is close to 100%.

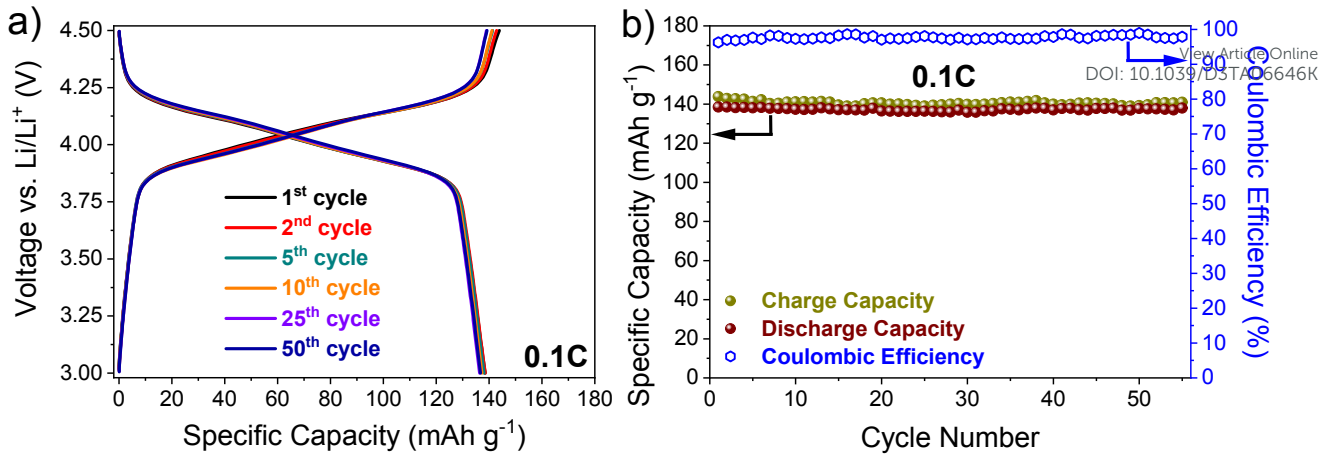

Figure 5. (a) Charge/discharge curves recorded at 0.1C. (b) Capacity values as a function of the cycle number obtained at 0.1C. LMO-Cl/Li cell.

The rate performance at different C-rates, from 0.1C to 100C with 10 cycle stages for each rate, are shown in Fig. 6a. Between 0.1C and 5C, the capacity values decrease very slowly from 140 to 135 mAh g^{-1}, respectively. From 10C and up to 100C, the highest tested rate, the decrease in capacity values is more pronounced, about 125, 115, 95 and 50 mAh g^{-1} obtained at 10C, 20C, 50C and 100C, respectively. As for the charge/discharge profiles in Fig. S6, the polarisation between the two curves increases in parallel to the rate, being more pronounced at 10C and especially at 50C and 100C. When the cell returns to 0.1C, the electrode virtually recovers the initial capacity value. This behaviour, together with the excellent capacity retention in the eleven stages analysed, is a clear sign of the good reversibility properties of reactions (1) and (2).

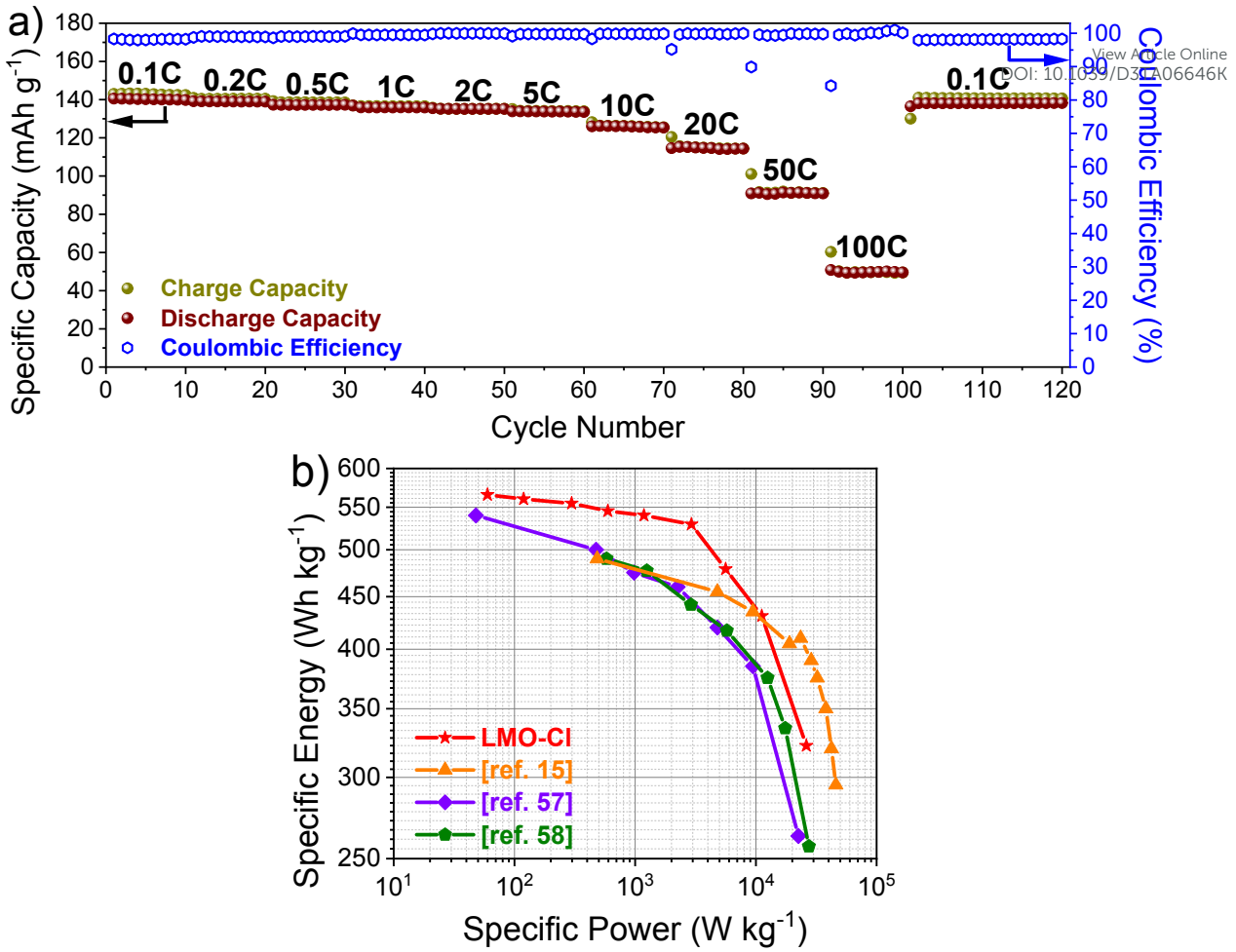

Figure 6. (a) Capacity values obtained in rate capability regime. (b) Ragone plot, along with the other three reported in the literature. LMO-Cl/Li cell.

The cycling properties of the electrode were complemented by its behaviour under prolonged cycling conditions. For this, different rates from 0.5 to 100C were chosen with cycle numbers of 500 (0.5 and 1C), 1000 (5 and 10C), 2.500 (50C), and 10000 (100C). The capacity values as a function of the cycle number are shown in Figs. 7 a–d for the first four rates and in Fig. S7 a and S7 b at 50C and 100C, respectively. The initial discharge capacities at 0.5C, 1C, 5C, and 10C are very similar, between 139 and 127 mAh g^{-1}. They show very similar values for both capacity retention, between 96 and 98%, and coulombic efficiency, close to 100%, hence the difficulty of plotting them in the same figure. At 50C, the initial capacity is still high, 120 mAh g^{-1} and up to 500 cycles. The capacity retention is also high, 87%, but after that, a more pronounced drop in capacity is observed that slows down after 1000 cycles, ending the 2500 cycle test with a capacity retention of around 50%. Although at 100C, the spinel still delivers a relatively high initial capacity, 80 mAh g^{-1}, the capacity retention worsens. At

View Article Online
DOI: 10.1039/D3TA06646K

about 300 cycles, a continuous drop is detected up to about 25 mAh g^{-1} at 2000 cycles, a value that stabilises in the remaining 8000 cycles resulting in 31% of capacity retention. The charge/discharge profiles are shown in Figs. S8 a−f. From 0.5 to 10C, Figs. S8 a−c, the profiles maintain the presence of the two pseudo-plateaus, with small polarisations between the different curves, direct proof of the good reversibility of reactions (1) and (2) in the short times for the implementation of both processes. For 50 and 100C, the polarisation between the charge/discharge curves is much greater, Figs. S8e and S8f, and the two plateaus are virtually unidentifiable.

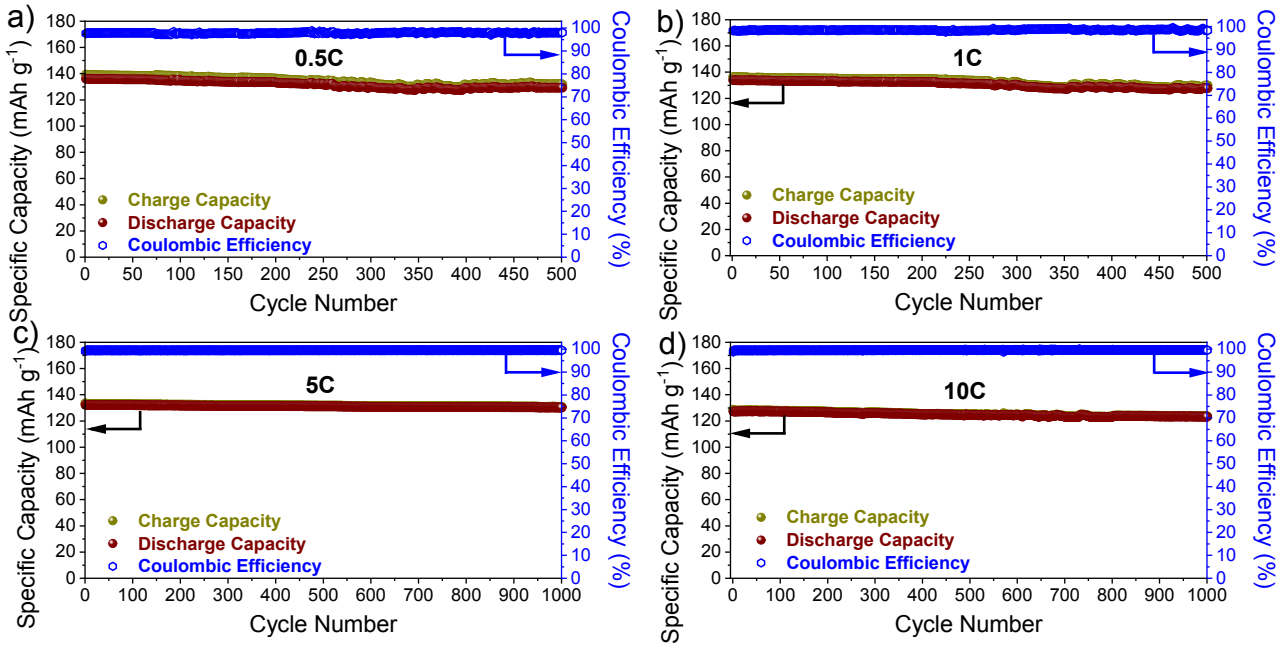

Figure 7. Capacity values as a function of cycle number obtained at C/2 (a), 1C (b), 5C (c) and 10 C rate (d) for LMO-Cl/Li cell.

Table S1 shows the values of the capacities found both in the prolonged cycling measurements and under the rate capability regime for the $LiMn_2O_4$ spinel reported in the last decade, taking as selection criteria several conditions-namely, the spinel has been subjected to a high number of cycles (200 or more), high rates were used, and the voltage window was 4.5−3.0 V. The results obtained in long-term cycling for our spinel reveal higher values of both initial capacity and capacity retention for rates between 1C and 10C, being outstanding for the excellent maintenance of capacity during a high number of cycles, between 97−95%. The conclusions are similar in the rate capability test. For rate values between 1C and 20C, our spinel shows the highest capacity values.

View Article Online
DOI: 10.1039/D3TA06646K

As for the specific energy and power values of the cells listed in Table S1, only in refs.[15,57,58] (included in Supplementary materials) are the values calculated from Ragone plots. To compare them with our spinel, the conversion of rate capability values of Fig. 6a in a Ragone plot is shown in Fig. 6b together with those of the three previous refs. For moderate specific power values, up to around 9000 W kg^{-1}, our spinel delivers the highest specific energy. For higher power values, only the spinel reported by Lee et al.[15] presents better performance. This spinel is also defective in Mn, $Li_{1.02}Mn_{1.98}O_4$. Also, it has two very different properties, coating with C and nanometric particle size (below 30 nm). Nevertheless, that obtained in the form of carbon-coated single-crystal nanoparticle clusters has higher power. However, a drastic power reduction is observed when the spinel undergoes rapid cooling after the carbon formation from glucose (quenched single crystal nanoparticle clusters). Regarding the spinels reported by Lu et al.[57] and Deng et al.[58], both are stoichiometric and have a morphology based on porous pseudo-spherical conglomerates of primary particles. Both have very similar Ragone plots but with much worse performances.

To shed additional light on the factors responsible for the excellent performance of the spinel electrode, cyclic voltammetry and impedance measurements were recorded. Fig. 8a shows several CV curves recorded at 0.1mV s^{-1}, with two pairs of well-separated oxidation peaks located at 3.95 and 4.15 V and the corresponding reduction peaks located at 4.11 and 3.90 V. Both have good correspondence with the two plateaus observed in charge/discharge galvanostatic curves, Fig. 5a. These features together with the small polarisation, hardly 0.04−0.05 V, between the oxidation and reduction peaks and discharge are consistent with the good reversibility of reactions (1) and (2). Fig. 8b shows the EIS spectra carried out at the OCV condition of the cell and upon CV. The spectra consisted of two depressed semicircles in the high to medium-frequency region and a straight line in the low region. In the high-frequency region, the intercept at Z' corresponds with the electrolyte resistance, and the semicircle is associated with the electrode/electrolyte film resistance (R_f). The semicircle in the middle-frequency range is related to the charge/transfer resistance (R_{ct}), and the inclined at low frequencies region depicts the Warburg impedance (Z_w) associated with Li^+ diffusion

View Article Online
DOI: 10.1039/D3TA06646K

in the $LiMn_2O_4$ particles.[59] The equivalent circuit used for fitting the spectra is drawn inside the figure, and the results obtained are included in Table 3. Apart from the negligible variation of R_e, the most notable feature is the significant decrease in the resistance of the electrode when cycling (around un 94%), among the smallest values reported in the literature.[17,60,61]

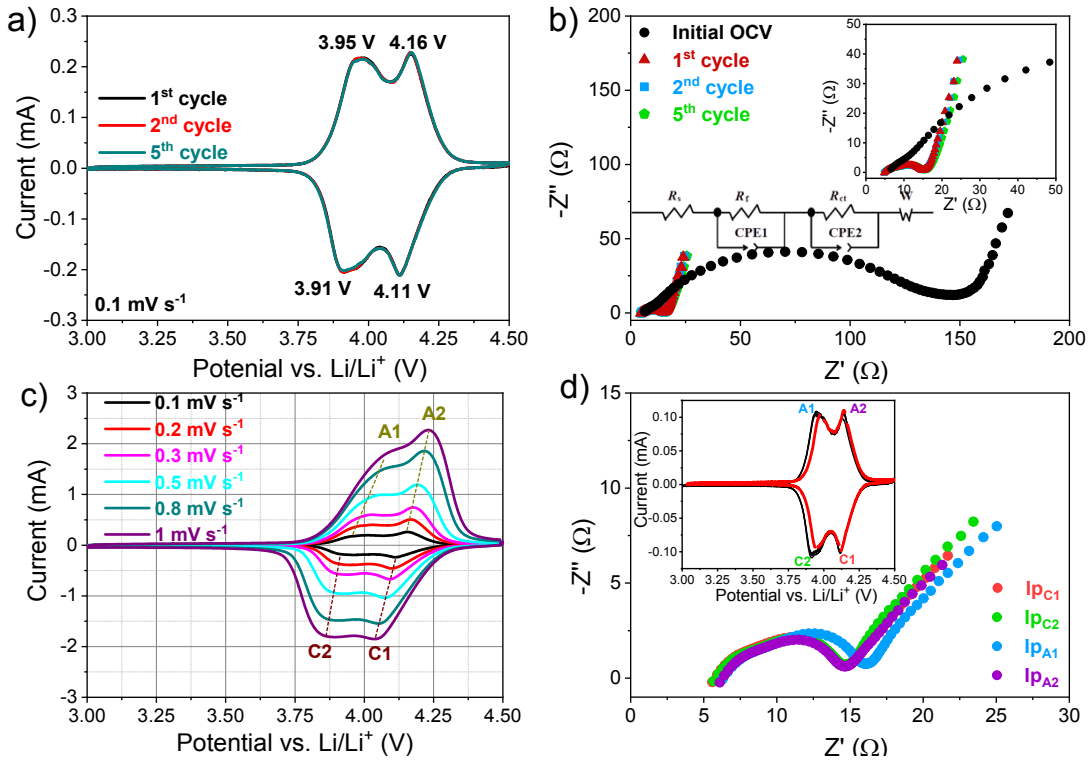

Figure 8. (a) CV curves recorded at 0.1 mV s^{-1}. (b) ES spectra recorded at OCV and after 1st, 2nd, and 5th voltammetric. (c) CV curves recorded at different scan rates from 0.1 to 1 mV s^{-1}. (d) Insert: cut-off points to further record the EI spectra after subjecting the cell to two voltammetric cycles at a scan of 0.05 mV s^{-1}. EI spectra obtained at the cut-off points. LMO-Cl/Li cell.

Table 3. Fitting results of the EI spectra (values in Ω) for LMO-Cl/Li cell.

Cell condition	R_e	R_f	R_{ct}	$R_t = R_f + R_{ct}$
OCV	5.4	68.4	66.4	134.8
After 1 CV cycle	5.3	5.0	3.1	8.1
After 2 CV cycles	5.3	3.2	4.9	8.1
After 5 CV cycles	5.3	5.1	3.4	8.5

View Article Online
DOI: 10.1039/D3TA06646K

The Li transport properties can be evaluated from the shifts of the redox peaks of the CV curves recorded at different scan rates, Fig. 8c. The diffusion coefficient D ($cm^2\ s^{-1}$) can be calculated according to the classical Randles−Sevcik equation:

$$I_{peak} = 0.4463zFAC\left[\frac{zF\nu D_{CV}}{RT}\right]^{1/2} \quad (3)$$

where I_{peak} is the peak current (A), z is the number of exchanged electrons of the electrochemical reaction, F is the Faraday constant (96 485 C mol^{-1}), A is the geometric area of the electrode (1.54 cm^2), C is the estimated Li^+ concentration in the electrode volume (mol cm^{-3}), ν is the scan rate (mV s^{-1}), D is the diffusion coefficient ($cm^2\ s^{-1}$), R is the gas constant (8.314 J K^{-1} mol^{-1}), and T is the temperature (298 K). Through equation (3), the D_{Li}^+ values of the LMO-Cl sample can be obtained from the slope of I_{peak} vs. $\nu^{1/2}$, as shown in Fig. S9, and they are listed in Table 4, where the labels A1 and A2 correspond to the anodic peaks, while C1 and C2 refer to the cathodic ones. The values are around 10^{-10} $cm^2\ s^{-1}$ with minimal variations between the different stages, both in the oxidation and reduction processes. The values are among the highest reported values by CV, ranging from 10^{-9} to 10^{-13} $cm^2\ s^{-1}$ because there are multiple factors which affect the measurement, including particle morphology and electrode geometry.[62]

The Li^+ diffusion coefficient was also calculated from the Warburg region[63] according to Equation 4:

$$D_{EIS} = \frac{1}{2}\left[\frac{RT}{z^2F^2CA\sigma}\right]^2 \quad (4),$$

where R, T, z, F, C and A have the same meanings as described in Eq. (3), and σ is the Warburg coefficient. D_{Li}^+ coefficients were calculated on the fourth CV curve by stopping at the positions A1, A2, C1, and C2 followed by the EIS spectra collected in Fig. 8d. The curve shape is similar to those of Fig. 8b after cycling and only that corresponding to the first oxidation peak, A1, shows slightly higher Z_{re} and Z_{im} values. From the Z vs $\omega^{-1/2}$ plots, Fig. S10, the σ coefficient was calculated. D_{Li}^+ values are shown in Table 4. The values obtained, *ca.* 10^{-10} $cm^2\ s^{-1}$, are like those calculated by CV, and there are no significant changes in the stages of the redox processes undergone by the electrode either. The use of EI spectra to evaluate D in $LiMn_2O_4$ is less common than using the CV technique.

View Article Online
DOI: 10.1039/D3TA06646K

The values found oscillate between 10^{-13} and 10^{-15} cm^2 s^{-1},[18] several orders of magnitude lower than that measured in our spinel. It is not the objective of this article to delve into the origin of these differences but simply to highlight the good Li-ion diffusion properties in our spinel, regardless of the electrochemical technique used for their evaluation. The good transport properties could be associated with the excess of Li and the defects induced in the structure. Using first-principles calculations Xiao et al.[29] found that the Li excess enhances Li ion diffusivity and Li et al.[30] concluded that antisite defects, i.e., LiMn, decreased the Li diffusion barriers.

Table 4. Li-ion diffusion coefficients of LMO-Cl sample.

Step reaction	D_{Li^+CV} (cm^2 s^{-1})	D_{Li^+EIS} (cm^2 s^{-1})
C1	$4.8 \cdot 10^{-10}$	$2.8 \cdot 10^{-10}$
C2	$4.7 \cdot 10^{-10}$	$1.6 \cdot 10^{-10}$
A2	$5.0 \cdot 10^{-10}$	$1.6 \cdot 10^{-10}$
A1	$7.3 \cdot 10^{-10}$	$3.2 \cdot 10^{-10}$

The post-mortem analysis of the cycled electrode, both from a structural and electrochemical point of view, is a good tool to help gain a better understanding of the electrode performance. The CV curves of the electrode at a scan rate of 0.1 mV s^{-1} in the potential range of 3.0−4.5 V, and the curves after cycling at 10C for 1000 cycles are shown in Fig. S11a. Their shapes are identical to those of the electrode before cycling, Fig. 8a. There are two couples of clearly separated oxidation and reduction peaks with even lower polarisations (*ca.* 0.02 V). Also, the shape of the EIS spectra of the same electrode recorded after the CV curves, Fig. S11b, is like the uncycled electrode and can be fitted to similar equivalent circuits. The *R* values obtained from the fitting are shown in Table S2. The R_e values are somewhat higher, probably associated with a slight electrolyte deterioration during cycling, but the evaluated resistances of the two depleted semicircles are somewhat lower, which justifies the lower polarisation observed in the redox processes. Our results differ from those found by Tomon et al.[17] in a core-shell LMO electrode cycled for 1000 cycles at 1C. They observed a significant increase, ca. 25%, in the value of the R_{ct}, already elevated after the first cycle, 78 Ω. Considering the

View Article Online
DOI: 10.1039/D3TA06646K

explanation proposed to explain this increase, partial dissolution of Mn in the electrolyte, it would mean that this feature is hardly relevant in our electrode.

Figures S12a,b show an SEM image of the LMO-Cl electrode before and after disassembling from the cell used for rate capability measurements. It is worth noting the little alteration undergone after the prolonged cycling, 120 cycles, and the multiple rate changes to which it has been subjected. After cycling, the polyhedral particle morphology is maintained, indirect proof that the stresses suffered by the particles in the successive processes of de-insertion/insertion of Li^+ have hardly affected the spinel structure, thus preventing particle pulverisation. This was further confirmed by the XRD pattern of the electrode after cycling, as shown in Fig. S12c. All the LMO peaks before cycling clearly appear after cycling with hardly any changes in their intensities or the 2θ angle, results that confirm the virtual maintenance of the spinel structure. The new observed peaks are assignable to the electrode additives, carbon black at around 26º in 2θ and binder, peaks at the left-hand side of (111) spinel reflection. The XRD pattern is different from the one found by Deng et al.[58] in an electrode after 500 cycles at 2C. In that XRD pattern, they detected substantial changes in the intensity of the peaks. The authors suggested that no phase transition from the cubic phase to the tetragonal phase was observed, and the structural stability of the LMO spinel was good. Our results go further, showing excellent maintenance of the stability of this LMO spinel during the prolonged cycling to which it was subjected. Similar results to those found in X-rays show the Raman spectra before and after cycling the spinel, characterized by the presence of a strong band around 620 cm^{-1} and a group of bands between 200 and 500 cm^{-1} with weaker intensity and consistent with its cubic structure, Fig. S12d.[64] After cycling the electrode, the changes undergone by the spectrum are negligible, another test which corroborates the excellent maintenance of the stability of this LMO spinel during the prolonged cycling to which it was subjected. XPS was also used as a complementary technique to characterize the Mn environment in the cycled electrode. In this case, the cell was only cycled for 25 cycles at 0.1C (average capacity value 138 mAh g^{-1}) and the cell was cut off discharged. The elements identified in the survey spectrum, Fig. S13a, are the same as before cycling, except Cl which is not

View Article Online
DOI: 10.1039/D3TA06646K

detected. Regarding the Mn 2*p* photoemission signal showed in Fig. S13 b and c, respectively, compared with the spectrum before cycling and that of the LMO-C sample (Fig. 4 a,b), the differences are negligible and, as noted, it is less useful for discussing the oxidation state of Mn. The photoemission signal Mn 3*s* is more appropriate and ΔE between the two peaks hardly varies when discharging the battery after the 25 cycles tested. This means that the average valence of Mn remains practically the same, calculated around 3.67 before cycling.[49]

3.2.2 Full-cells

The huge bibliography published on the electrochemical behaviour of LMO in half-cells contrasts with the few reports published on full-cells (especially in coin cell type), and the use of $Li_4Ti_5O_{12}$ spinel[9,65–70] predominates over graphite[16,72,73] as the anode. The origin of this could lie in the results of Zhang et al.[9], who found poorer performance when cycled against MCMB with a capacity loss of around 15% after 100 cycles, while the cell with LTO had almost no fade capacity. This was associated with a higher amount of Mn deposited on an MCMB anode, 320 ppm versus 300 ppm on LTO after 100 cycles. However, the greater deposition of Mn in the half-cell is striking, *ca.* 400 ppm, when the expected behaviour *vs* Li electrode is equal or better. Moreover, in commercial-type configurations, *vgr.* 18650 type, a $LiMn_2O_4$ battery with MCMB or graphite as the anode[17,74,75] shows high values of capacity retention over a high cycle number. There have been several reasons for opting for graphite as the full-cell anode here. It is cheaper than Ti spinel, it is around 4 times smaller, supplies a higher voltage, and satisfies most of the requirements of an ideal anode; hence, it is preferred for commercial LIBs.[16]Also, our group is more familiar with this material.[76-79]

Before commenting on the electrochemical results of LMO full cells, we will briefly describe the behaviour of MCMB vs Li. This, together with the results already described for LMO vs Li half-cell, allows a calculation of the relative content of active material in both electrodes. The charge/discharge curves recorded at 0.1C (1C = 372 mA g^{-1}) are shown in Fig. S14a. The shape is that expected for this graphitic carbon, a fast fade in the potential as Li is intercalated into the graphite structure

View Article Online
DOI: 10.1039/D3TA06646K

followed by a plateau below 0.2 V, a little polarisation between both curves, and a small irreversible capacity, enough reasons to use it without subjecting it to a pre-lithiation process. The evolution of the capacity values as a function of the number of cycles is shown in Fig. S14b. As can be observed, the MCMB electrode exhibits good capacity retention with an average capacity value of 300 mAh g^{-1}. This value, together with that obtained for the spinel (140 mAh g^{-1}), has been used to calculate the N/P ratio, the value of which should be close to 1, hence the value of 1.03 used for the full-cell assembly (LMO: 3.1 mg cm^{-2}, MCMB: 1.5 mg cm^{-2}). Regarding the behaviour under the rate capability regime, Figs. S15 a and b, it is worse than that found in the spinel because the capacity decreases sharply from moderate rate values, 1C. At 10C, the capacity is barely 50 mAh g^{-1}, and at 50C, it is almost zero. However, when returning to 0.1C, the capacity is close to the initial one, around 300 mAh g^{-1}.

The rate capability results of the full cell recorded under the same conditions as those used in the half-cell, from 0.1C to 100C, are shown in Fig. 9a. Between 0.1C and 2C, the average capacity values decrease slowly from 130 to 116 mAh g^{-1} (referred to LMO-Cl electrode), respectively, between 8% and 15% capacity loss compared to half-cell values. The capacity fade is more pronounced for higher C values, and at 100C the delivered capacity is hardly 4 mAh g^{-1}, *ca*. 92% lower than that of the half-cell. As for the charge/discharge profiles, Fig. S16, the polarisation between the two curves increases in parallel to the rate, but the two stages of the electrochemical reaction are less well defined. When it returns to 0.1C, the electrode approaches the initial capacity value, *ca.* 120 mAh g^{-1}. This behaviour, together with the excellent capacity retention in the eleven stages analysed, is a clear sign of the good reversibility properties of reactions (1) and (2). Prolonged cycling tests were carried out at 1C and 10C, Figs. 9 b, c. At these rates and especially at 10C, the plateaus are not discernible, Figs. S17 a and b, due to the overpotential and transport limitation of the electrodes, particularly the MCMB electrode. At 1C, the initial capacity, C_i, is around 130 mAh g^{-1}. It slowly fades to 90 mAh g^{-1} after 200 cycles. At 10C, the delivered capacity continues to be high, 100 mAh g^{-1}, progressing from 77 to 40 mAh g^{-1} at 200 and 2000 cycles, respectively.

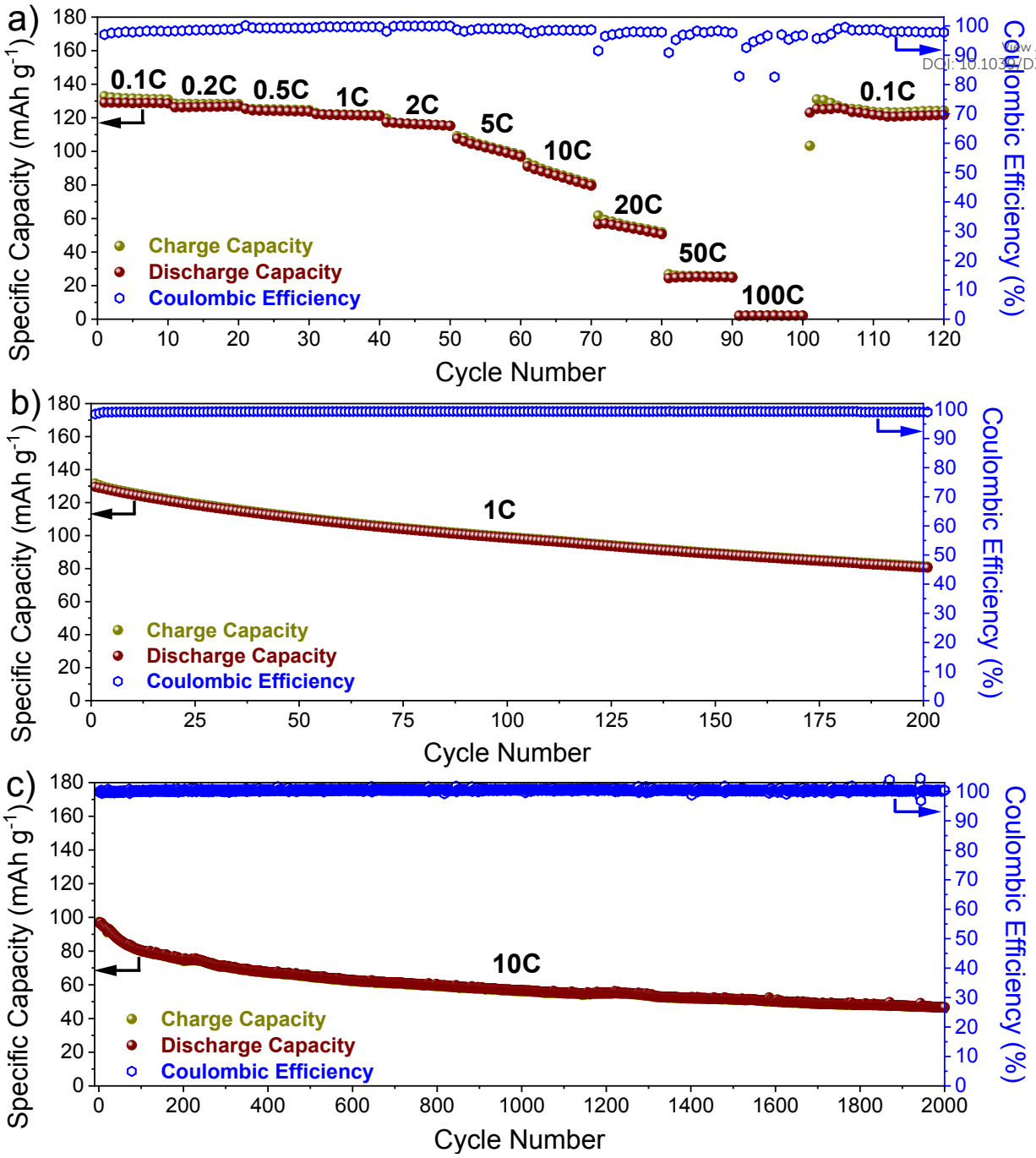

Figure 9. Variation of capacity values as a function of cycle number of LMO-Cl/MCMB cell: (a) Rate capability regime, (b) 1C, (c) 10C rate.

Table 5 shows some properties of the few articles on coin-type LMO-graphite full cells found in the literature and in which only measurements in prolonged cycling are provided. Of the three articles, the N/P capacity ratio used is only quoted in two of them, but it is higher than the optimum of 1. Regarding the current used, there is also doubt about the real value used in two of the articles. Rashid and Gupta[73] adopt a criterion more commonly used in commercial batteries, where the capacity is

View Article Online
DOI: 10.1039/D3TA06646K

referred to in terms of mAh. Nevertheless, we have calculated the discharge value for our cell in these units, and the values at 1C were 0.40 and 0.28 mAh for cycles 1 and 150, respectively. If we consider that the weight of the active material used in ref.[73], a total of 11.6 mg cm^{-2} between cathode and active, is 2.58 greater than that of our cell, the capacity values, 1.03 and 0.79 mAh in cycles 1 and 100, respectively, are very similar, with 76% capacity retention (see Table 5). It is more difficult to compare our cell with the one reported by Jeon et al.[72] because the measurement conditions are very different: a wider potential window, another type of graphite and prelithiated, and a lower rate. Despite these apparently more favourable conditions, the performance of our cell is better. We find that the cells described by Selvamani et al.[16] are more similar, although the value of the N/P ratio is not quoted. In the half-cell results reported by these authors, we already pointed out the better behaviour of our spinel compared with the core-shell and pristine LMOs (see Table 2). The conclusion about full cells is the same, our spinel delivers higher capacity values and exhibits better capacity retention.

View Article Online
DOI: 10.1039/D3TA06646K

Table 5. Performance of LMO coin-type full cells reported in literature The properties of our LMO full-cell are also included for comparison.

Cell	N/P ratio	Long Term Cycling					Rate Capability		Ref.
		C (mA g^{-1})	C_i (mAh g^{-1})	Nº Cycles	Rate (C)	C. R. (%)	Rate (C)	C_{av}	
Polyhedral $Li_{1.06}Mn_{1.94}O_4$ microparticles/MCMB	0.94	148	130 (0.40) 100	150 (0.28) 2000	1 10	70 40	1 2 5 10 50 100	122 116 102 85 53 23	**This work**
Carbon core-shell LMO(comm.)/MCMB*		100	71	1000	0.75	50			16
Pristine LMO/MCMB			70	1000		35			
LMO(comm.)/Graphite (prelithiated)	1.7	N/A	200	100	0.15	50			72
LMO(comm.)/MCMB	2.0	N/A	1.08** 1.0**	100 100	1 2	76 63			73
LMO(comm.)/LTO(+) (comm.)	1.3	130	94.7	1000	1(+)	81			69
LMO+MCMB(50%)/LTO	_	N/A	60	600(++)	N/A	80			70
Porous LMO microspheres/LTO nanorods		N/A	40	1000	N/A	60			65
LMO(comm.)/C-$Li_3Nd_3W_2O_{12}$		100	130 95	100 300	71 83	1 2	2 4 8	100 80 60	80

(*) Voltage window:4.5–2.0 V. (**) Capacity values in mAh. (+) Performed at 45 ºC; cycles 1 and 2 at C/10. (++) Deep cycling mode (1.5–3.4 V). C_i: Initial discharge capacity. C_{av}: Average capacity. C. R.: capacity retention.

Although the chemical and electrochemical properties of the LTO spinel are very different from those of the MCMB, comparing their behaviour in full cells against the LMO spinel corroborates the good properties of our spinel as an LIB electrode. Despite the greater number of reports on LMO-LTO cells already cited, an exhaustive description of the experimental conditions of measurements is

View Article Online
DOI: 10.1039/D3TA06646K

scarce. Hence, only a few, also with limited information, have been included in Table S1. Only Ha et al.[69] provided enough data to establish a more reliable comparison, but they cycled at a higher temperature, 45 ºC. At the only rate tested, 1C (130 mA g^{-1}, somewhat lower than ours), the capacity retention is higher, and the delivered capacity is lower. The other LMO/LTO full cells, with the LMO spinel well mixed with MCMB to improve the conductivity[70] or with special morphology[65] in which some experimental data are missing, behave worse. An anodic material that draws attention due to its different structure and composition is the mixed oxide $Li_3Nd_3W_2O_{12}$ with a garnet-like structure and coated with C.[80] Its electrochemical performance against LMO is like that of our cell with MCMB. However, the potential difference vs Li is small, and its theoretical specific capacity is significantly lower, 106 compared to 372 mAh g^{-1} for graphite.

The specific energy and power values evaluated from the rate capability measurements are shown in Fig. S18. The values are lower than those calculated for the LMO/Li cell. This difference becomes more pronounced for high rate values, starting at 10C and is attributable to the limited electrochemical response of the MCMB for high current values. None of the reports on full cells with MCMB as the anode, collected in Table 5, evaluated the values of energy and specific power released, so it is not possible to carry out a comparative study. We have only found one study, although with different anodic ($ZnFe_2O_4$−C) and cathodic ($LiFePO_4$−MWCNT) materials but using conditions comparable to ours, showed rates between 0.5 and 20C (values referred to the cathode).[81] The energy and specific power values measured at 0.5 and 1C were 135 Wh kg^{-1} # 300W Kg^{-1} and 64 Wh kg^{-1} # 3000 W kg^{-1}, respectively. These values are much lower than ours, 480 Wh kg^{-1} # 330W Kg^{-1} and 200 Wh kg^{-1} # 10000 W kg^{-1}, for the same rates, respectively. Even when the anode is prelithiated with high capacity values, 600 mAh g^{-1}, the values are still significantly lower (180 Wh kg^{-1} # 350 W kg^{-1} and 90 Wh kg^{-1} # 3720 W kg^{-1} for 0.5 and 1C, respectively).

Unlike the galvanostatic curves, the two stages in the CV curves, defined by the reactions (1) and (2) both in the discharge and the charge of the redox process, are clearly distinguishable, Fig. S19a, but the peaks are wider compared with those of the half-cell. The result is a greater overlap that makes a

View Article Online
DOI: 10.1039/D3TA06646K

precise calculation of the polarisation values difficult, although they are somewhat like those found in the half-cell, ca. 0.04 V. The EIS technique was also employed in LMO/MCMB cells to analyse the evolution of the cell impedance at OCV and after recording the 1st, 2nd, and 5th CV curves (in the charge state, 4.5V), Fig. S19b. Compared with half-cells, Fig. 8b, the two depressed semicircles in the high to medium frequency region are better defined, particularly the semicircle associated with the electrode/electrolyte film resistance (R_f). The fitting values of the different components of the equivalent circuit are shown in Table S3. It is worth noting the decrease observed in the cell values at OCV and a somewhat less pronounced increase in the electrolyte resistance for which we do not have a convincing explanation. However, the values are comparable to a few available in the literatue.[72] On the other hand, when the cell is cycled, the behaviour of the EIS spectra is similar, with a decrease in resistance, giving values close to those measured in half cells.

The diffusion coefficient of Li^+ in the full cell was calculated from the redox peaks of the CV curves recorded at different scan rates, Fig. S20a, from Eq. (3) previous calculation of the slope of the I_{peak} vs. $v^{1/2}$ plot (Figs. S20 b, c). The values are listed in Table S4 and, as in the half-cells, they are in the range of 10^{-10} cm^2 s^{-1}, but they are slightly lower in all the stages of the redox process. The Li^+ diffusion coefficients were calculated from the Warburg impedance by applying Eq. 4, following the same procedure as in the half-cell, first two voltammetric cycles at 0.05 mV s^{-1} for activation followed by cuts in the voltammetric curve at different positions, Fig. S21a, and then recording the EI curve and then recording the EI curve at each of the four cut-off points, Fig. S21b. The σ coefficient of Eq. 4 was obtained from the slope of Z *vs* $\omega^{-1/2}$ plots, Figs. S21 c–f. The D_{Li^+} values shown in Table S4 are like those calculated by CV *ca.* 10^{-10} cm^2 s^{-1} and hardly change in the different stages of Li^+ removal and insertion in the spinel structure. It is worth noting that the similarity between these values and those collected in Table 4 are indicative of the good transport properties of the spinel regardless of the anode used.

4. Conclusions

View Article Online
DOI: 10.1039/D3TA06646K

We have successfully synthesised a highly crystalline, microsized $LiMn_2O_4$ spinel with a polyhedral shape using Cl_2 as an oxidising agent to enhance the conversion of Mn^{3+} to Mn^{4+}. In this way, the two inherent properties of Mn^{3+} that affect the spinel stability as electrodes in LIB, the structure distortion associated with the Jahn-Teller effect and its disproportion in Mn^{4+} and Mn^{2+} are mitigated, and the main reasons for the solubility of spinel in the electrolyte are mitigated**.** The XRD results confirmed the deficiency in Mn^{3+}. The good agreement of the mean oxidation state of Mn, ca. 3.67, calculated from the XR patterns and the XPS spectra, is noteworthy. The spinel showed outstanding Li^+ insertion/de-insertion properties, with remarkable high-rate capability and long-term cyclability without the need for special treatments to its conductivity and/or modify its surface and texture. In a half-cell configuration, the electrode delivers a specific capacity of 140 mAh g^{-1} at 0.1C charge/discharge, close to the theoretical capacity of its spinel content and a capacity loss of hardly 0.02% on cycling. At 10C, the deliverable discharge capacity is close to 130 mAh g^{-1}, and the capacity retention approaches 96% for up to 1000 cycles. Even after 1000 cycles at 50 C, the spinel delivers 50 mAh g^{-1}. In fact, the results of long-term cycling tests of our spinel revealed higher values of both initial discharge capacity and capacity retention for current rates between 1C to 10C, compared to those reported in the literature, being noteworthy for the excellent maintenance of capacity during a high number of cycles. Post-mortem studies of the electrode from the rate capability test (from 0.1 to 100C and again to 0.1C, thus subjected to multiple current changes) revealed maintenance of the spinel structure as well as its polyhedral morphology, a direct proof of the remarkable stability of the spinel during the many processes of Li extraction and insertion undergone. As expected, the electrochemical performance is also outstanding in full-cell configuration, although worse than against Li. MCMB, a graphitized carbon used in commercial batteries, was selected as the anode. The cell in the rate capability regime behaves satisfactorily from 1 to 10C, releasing an average capacity of 122 and 85 mAh g^{-1}, respectively. In prolonged cycling, the differences in performance with respect to the halfcell configuration become somewhat more pronounced. However, the

conclusion is the same, our spinel performs better than other spinels reported in the literature. Two intrinsic complementary properties of this spinel could explain its good electrochemical properties and cycling stability. Firstly, a well-defined microstructure leading to octahedral microparticles with surfaces aligned to crystalline orientations that hinder the dissolution of Mn. Although the presence of an excess of Li barely affects the typical octahedral geometry of the microparticles, at the atomic level the structural changes deserve to be highlighted. On the one hand, it decreases the Mn^{3+} content, responsible for JT distortion and the main cause of spinel instability. But it also causes a cationic disorder in the structure (excess Li in the Mn positions and antisite defects) that break the symmetry of the $M^{3+}O_6$ octahedra and block the Jahn-Teller distortion both individually and collectively. Furthermore, partial, and total edges dislocations have been detected in the HRTEM images, where not only the Mn and Li ions modify their environments and coordination, but also the positions of the O atoms are affected. These defects can reduce the inhomogeneous expansion/contraction in volume and relax the strain generated during the intercalation/de-intercalation process and enhance the Li-ion mobility.[82]

Declaration of Competing Interest

The authors declare that they have no known competing financial interests or personal relationships that could have appeared to influence the work reported in this paper.

CRediT authorship contribution statement

Fernando Luna: Data curation, Formal analysis, Investigation, Writing – original draft. Lucía Barbosa: Data curation, Investigation, Writing – original draft, Supervision. Alvaro Y. Tesio: Data curation, Writing – review & editing. Alvaro Caballero: Methodology, Supervision, Writing – review & editing, Funding acquisition. Julián Morales: Conceptualization, Methodology, Supervision, Validation, Writing – review & editing.

View Article Online
DOI: 10.1039/D3TA06646K

Acknowledgements

This research was funded by Ministerio de Ciencia e Innovación MCIN/AEI/10.13039/501100011033 (Project PID2020-113931RB-I00), European Union "NextGenerationEU"/PRTR (Project PDC2021-120903-I00), Junta de Andalucía (FQM-175) and CONICET (PIP 2021-2023 GI-11220200100704CO). AYT thanks to the UCO program "Ayudas para la recualificación del sistema universitario español, Modalidad María Zambrano". The authors wish to acknowledge technical staff from the Instituto Químico para la Energía y el Medioambiente (IQUEMA) and Servicio Central de Apoyo a la Investigación (SCAI) of Córdoba University. We want to highlight the help provided by the X-ray Photoelectron Spectroscopy and X-ray Diffraction units of the SCAI of Málaga University, and a special thanks to Dr. Laura Leon Reina for her help in the interpretation and preparation of the XRD results.

References

1 M. M. Thackeray, *Prog. Solid State Chem.*, 1997, **25**, 1–71, DOI: https://doi.org/10.1016/S0079-6786(97)81003-5.

2 J. B. Goodenough and Y. Kim, *Chem. Mater.*, 2010, **22**, 587–603, DOI: https://doi.org/10.1021/cm901452z.

3 H. Xia, Z. Luo and J. Xie, *Prog. Nat. Sci. Mater. Int.*, 2012, **22**, 572–584, DOI: https://doi.org/10.1016/j.pnsc.2012.11.014.

4 Y. Huang, Y. Dong, S. Li, J. Lee, C. Wang, Z. Zhu, W. Xue, Y. Li and J. Li, *Adv. Energy Mater.*, 2021, **11**, 2000997, DOI: https://doi.org/10.1002/aenm.202000997.

5 D. Di Lecce, R. Verrelli and J. Hassoun, *Green Chem.*, 2017, **19**, 3442–3467, DOI: https://doi.org/10.1039/c7gc01328k.

6 M. M. Thackeray, E. Lee, B. Shi and J. R. Croy, *J. Electrochem. Soc.*, 2022, **169**, 020535, DOI: https://doi.org/10.1149/1945-7111/AC50DD.

7 Z. Iskandar Radzi, K. Helmy Arifin, M. Zieauddin Kufian, V. Balakrishnan, S. Rohani Sheikh Raihan, N. Abd Rahim and R. Subramaniam, *J. Electroanal. Chem.*, 2022, **920**, 116623, DOI:

https://doi.org/10.1016/j.jelechem.2022.116623.

8 M. M. Thackeray, *J. Am. Ceram. Soc.*, 1999, **82**, 3347–3354, DOI: https://doi.org/10.1111/j.1151-2916.1999.tb02250.x.

9 C. Zhang, J. Lu, A. Jeremy Kropf, T. Wu, A. N. Jansen, Y. K. Sun, X. Qiu and K. Amine, *Nat. Commun.*, 2013, **4**, 2437, DOI: https://doi.org/10.1038/ncomms3437.

10 A. Bhandari and J. Bhattacharya, *J. Electrochem. Soc.*, 2017, **164**, A106–A127, DOI: https://doi.org/10.1149/2.0101614jes.

11 B. Xu and S. Meng, *J. Power Sources*, 2010, **195,** 4971–4976, DOI: https://doi.org/10.1016/S0378-7753(99)00362-6.

12 H. Hayakawa, T. Takada, H. Enoki AND E. Akiba, *J. Mater. Sci. Lett.*, 1998, **17,** 811–812, DOI: https://doi.org/10.1023/A:1006682304966.

13 G. Singh, S. L. Gupta, R. Prasad, S. Auluck, R. Gupta and A. Sil, *J. Phys. Chem. Solid*, 2009, **70,** 1200–1206, DOI: https://doi.org/10.1016/j.jpcs.2009.07.001.

14 Z. Chen, Y. Qin, K. Amine and Y. K. Sun, *J. Mater. Chem.*, 2010, **20**, 7606–7612, DOI: https://doi.org/10.1039/c0jm00154f.

15 S. Lee, Y. Cho, H. K. Song, K. T. Lee and J. Cho, *Angew. Chemie - Int. Ed.*, 2012, **51**, 8748–8752, DOI: https://doi.org/10.1002/anie.201203581.

16 V. Selvamani, N. Phattharasupakun, J. Wutthiprom and M. Sawangphruk, *Sustain. Energy Fuels*, 2019, **3**, 1988–1994, DOI: https://doi.org/10.1039/c9se00274j.

17 C. Tomon, S. Sarawutanukul, N. Phattharasupakun, S. Duangdangchote, P. Chomkhuntod, N. Joraleechanchai, P. Bunyanidhi and M. Sawangphruk, *Commun. Chem.*, 2022, **5**, 54, DOI: https://doi.org/10.1038/s42004-022-00670-y.

18 Y. Lee, N. Kumada and M. Yoshio, *J. Power Sources*, 2001, **96**, 376–384, DOI: https://doi.org/10.1016/S0378-7753(00)00652-2.

19 Y. Shin and A. Manthiram, *J. Electrochem. Soc.*, 2004, **151**, A204, DOI: https://doi.org/10.1149/1.1634274.

20 T. Liu, A. Dai, J. Lu, Y. Yuan, Y. Xiao, L. Yu, M. Li, J. Gim, L. Ma, J. Liu, C. Zhang, L. Li, J. Zheng, Y. Ren, T. Wu, R. Shahbazian-Yassar, J. Wen, F. Pan and K. Amine, *Nat. Commun.*, 2019, **10**, 4271, DOI: https://doi.org/10.1038/s41467-019-12626-3.

21 Q. Liu, L. Zhong, Y. Guo, M. Xiang, C. Su, P. Ning and J. Guo, *J. Alloys Compd.*, 2021, **874**, 159912, DOI: https://doi.org/10.1016/j.jallcom.2021.159912.

22 X. Zeng, J. Wu and Q. Hu, *Micro Nano Lett.*, 2016, **11**, 789–791, DOI:

https://doi.org/10.1049/mnl.2016.0445.

23 E. Hosono, T. Kudo, I. Honma, H. Matsuda and H. Zhou, *Nano Lett.*, 2009, **9**, 1045–1051, DOI: https://doi.org/10.1021/nl803394v.

24 Y. L. Ding, J. Xie, G. S. Cao, T. J. Zhu, H. M. Yu and X. B. Zhao, *Adv. Funct. Mater.*, 2011, **21**, 348–355, DOI: https://doi.org/10.1002/adfm.201001448.

25 L. Xiong, Y. Xu, T. Tao and J. B. Goodenough, *J. Power Sources*, 2012, **199**, 214–219, DOI: https://doi.org/10.1016/j.jpowsour.2011.09.062.

26 Y. Yu, J. Guo, M. Xiang, C. Su, X. Liu, H. Bai, W. Bai and K. Duan, *Sci. Rep.*, 2019, **9**, 1–9, DOI: https://doi.org/10.1038/s41598-019-53494-7.

27 E. A. Velásquez, D. P. B. Silva, J. B. Falqueto, J. Mejía-López, N. Bocchi, R. Del Rio, J. Mazo-Zuluaga, R. C. Rocha-Filho and S. R. Biaggio, *J. Mater. Chem. A*, 2018, **6**, 14967–14974, DOI: https://doi.org/10.1039/c8ta02703j.

28 Y. Koyama, I. Tanaka, H. Adachi, Y. Uchimoto, and M. Wakihara, *J. Electrochem. Soc.*, 2003 **150**, A63−A67, DOI: https://doi.org/10.1149/1.1522720.

29 W. Xiao, C. Xin, S. Li, J. Jie, Y. Gu, J. Zheng and F. Pan, *J. Mater. Chem. A*, 2018, **6**, 9893–9898, DOI: DOI https://doi.org/10.1039/C8TA01428K.

30 X. Li, J. Wang, S. Zhang, L. Sun, W. Zhang, F. Dang, H. J. Seifert and Y. Du, *ACS Omega*, 2021, **6**, 21255−21264, DOI: https://doi.org/10.1021/acsomega.1c01162.

31 C. Dessemond, F. Lajoie-Leroux, G. Soucy, N. Laroche and J. F. Magnan, *Minerals*, 2019, **9**, 334, DOI: https://doi.org/10.3390/min9060334.

32 L. I. Barbosa, J. A. González and M. Del Carmen Ruiz, *Thermochim. Acta*, 2015, **605**, 63–67, DOI: https://doi.org/10.1016/j.tca.2015.02.009.

33 D. Di Lecce, L. Carbone, V. Gancitano and J. Hassoun, *J. Power Sources*, 2016, **334**, 146–153, DOI: https://doi.org/10.1016/j.jpowsour.2016.09.164.

34 H. M. Rietveld, *J. Appl. Crystallogr.*, 1969, **2**, 65–71, DOI: https://doi.org/10.1107/s0021889869006558.

35 R. D. Shannon and C. T. Prewitt, *Acta Crystallogr. Sect. B Struct. Crystallogr. Cryst. Chem.*, 1969, **25**, 925–946, DOI: https://doi.org/10.1107/s0567740869003220.

36 C. Fong, B. J. Kennedy and M. M. Elcombe, *Zeitschrift für Krist.*, 1994, **209**, 941–945, DOI: https://doi.org/10.1524/zkri.1994.209.12.941.

37 M. Yonemura, A. Yamada, H. Kobayashi, M. Tabuchi, T. Kamiyama, Y. Kawamoto and R. Kanno, *J. Mater. Chem.*, 2004, **14**, 1948–1958, DOI: https://doi.org/10.1039/b314810f.

38 P. Piszora, C. R. A. Catlow, S. M. Woodley and E. Wolska, *Comput. Chem.*, 2000, **24**, 609–613, DOI: https://doi.org/10.1016/S0097-8485(00)00060-7.

39 M. A. Limpert, E. A. Baroncini, E. J. Gritton, T. B. Atwater and E. D. Wachsman, *J. Power Sources*, 2022, **528**, 231225, DOI: https://doi.org/10.1016/j.jpowsour.2022.231225.

40 P. Strobel and B. Lambert-Andron, *J. Solid State Chem.*, 1988, **75**, 90–98, DOI: https://doi.org/10.1016/0022-4596(88)90305-2.

41 H. Liu, D. Qian, M. G. Verde, M. Zhang, L. Baggetto, K. An, Y. Chen, K. J. Carroll, D. Lau, M. Chi, G. M. Veith and Y. S. Meng, *ACS Appl. Mater. Interfaces*, 2015, **7**, 19189–19200, DOI: https://doi.org/10.1021/acsami.5b04932.

42 J. S. Kim, K. Kim, W. Cho, W. H. Shin, R. Kanno and J. W. Choi, *Nano Lett.*, 2012, **12**, 6358–6365, DOI: https://doi.org/10.1021/nl303619s.

43 R. A. Rodríguez, E. L. Pérez-Cappe, Y. M. Laffita, A. C. Ardanza, J. S. Salazar, M.Á. Santos, M. A. Frutis, N. D. S. Mohalem and O. L. Alves, *Solid State Ionics*, 2018, **324,** 77–86, DOI: https://doi.org/10.1016/j.ssi.2018.06.007.

44 J. F. Moulder, W. F. Stickle, P. E. Sobol and K. D. Bomben, *Handbook of X-Ray Photoelectron Spectroscopy*, Perkin-Elmer Corporation, Eden Prairie, Minesota, USA, 1992.

45 M. C. Biesinger, B. P. Payne, A. P. Grosvenor, L. W. M. Lau, A. R. Gerson and R. S. C. Smart, *Appl. Surf. Sci.*, 2011, **257**, 2717–2730, DOI: https://doi.org/10.1016/j.apsusc.2010.10.051.

46 L. Ben, H. Yu, B. Chen, Y. Chen, Y. Gong, X. Yang, L. Gu and X. Huang, *ACS Appl. Mater. Interfaces*, 2017, **9**, 35463–35475, DOI: https://doi.org/10.1021/acsami.7b11303.

47 R. P. Gupta and S. K. Sen, *Phys. Rev. B*, 1975, **12**, 15–19, DOI: http://link.aps.org/doi/10.1103/PhysRevB.12.15.

48 Y. Pei, C. Y. Xu, Y. C. Xiao, Q. Chen, B. Huang, B. Li, S. Li, L. Zhen and G. Cao, *Adv. Funct. Mater.*, 2017, **27**, 1604349, DOI: https://doi.org/10.1002/adfm.201604349.

49 S. M. Bak, K. W. Nam, C. W. Lee, K. H. Kim, H. C. Jung, X. Q. Yang and K. B. Kim, *J. Mater. Chem.*, 2011, **21**, 17309–17315, DOI: https://doi.org/10.1039/c1jm13741g.

50 R. R. Unocic, L. Baggetto, G. M. Veith, J. A. Aguiar, K. A. Unocic, R. L. Sacci, N. J. Dudney and K. L. More, *Chem. Commun.*, 2015, **51**, 16377–16380, DOI: https://doi.org/10.1039/c5cc07180a.

51 Z. Lu, X. Lu, J. Ding, T. Zhou, T. Ge, G. Yang, F. Yin and M. Wu, *Appl. Surf. Sci.*, 2017, **426**, 19–28, DOI: https://doi.org/10.1016/j.apsusc.2017.07.117.

52 A. J. Nelson, J. G. Reynolds and J. W. Roos, *J. Vac. Sci. Technol. A Vacuum, Surfaces, Film.*, 2000, **18**, 1072–1076, DOI: https://doi.org/10.1116/1.582302.

53 J. R. Croy, S. H. Kang, M. Balasubramanian and M. M. Thackeray, *Electrochem. commun.*, 2011, **13**, 1063–1066, DOI: https://doi.org/10.1016/j.elecom.2011.06.037.

54 L. Xiao, J. Xiao, X. Yu, P. Yan, J. Zheng, M. Engelhard, P. Bhattacharya, C. Wang, X. Q. Yang and J. G. Zhang, *Nano Energy*, 2015, **16**, 143–151, DOI: https://doi.org/10.1016/j.nanoen.2015.06.011.

55 K. Kubota, T. Kaneko, M. Hirayama, M. Yonemura, Y. Imanari, K. Nakane and R. Kanno, *J. Power Sources*, 2012, **216**, 249–255. DOI: https://doi.org/10.1016/j.jpowsour.2012.05.061.

56 C. S. Johnson, N. Li, J. T. Vaughey, S. A. Hackney and M. M. Thackeray, *Electrochem. commun.*, 2005, **7**, 528–536, DOI: https://doi.org/10.1016/j.elecom.2005.02.027.

57 J. Lu, C. Zhou, Z. Liu, K. S. Lee and L. Lu, *Electrochim. Acta*, 2016, **212**, 553–560, DOI: https://doi.org/10.1016/j.electacta.2016.07.013.

58 Y. Deng, Y. Zhou, Z. Shi, X. Zhou, X. Quan and G. Chen, *J. Mater. Chem. A*, 2013, **1**, 8170–8177, DOI: https://doi.org/10.1039/c3ta11563a.

59 R. Greef, R. Peat, L. M. Peter, D. Pletcher and J. Robinson, *Instrumental Methods in Electrochemistry*, Ellis Horwood Limited, Chichester, West Sussex, UK, Wiley & Sons, 1985.

60 W. Wen, B. Ju, X. Wang, C. Wu, H. Shu and X. Yang, *Electrochim. Acta*, 2014, **147**, 271–278, DOI: https://doi.org/10.1016/j.electacta.2014.09.115.

61 S. Wang, H. Liu, M. Xiang, J. Guo, W. Bai, H. Bai, X. Liu and C. Su, *New J. Chem.*, 2020, **44**, 10569–10577, DOI: https://doi.org/10.1039/d0nj01290d.

62 M. D. Chung, J. H. Seo, X. C. Zhang and A. M. Sastry, *J. Electrochem. Soc.*, 2011, **158**, A371, DOI: https://doi.org/10.1149/1.3549161.

63 X. Zhang, B. Peng, L. Zhao, G. Wan, F. Wang, S. Zeng, H. Zhang**,** J. Ding and G. Zhang. *ACS Appl. Mater. Interfaces*, 2022, **14**, 16204–16213, DOI: https://doi.org/10.1021/acsami.2c00533.

64. C. V. Ramana, M. Massot and C. M. Julien, *Surf. Interface Anal.*, 2005, **37**, 412–416, DOI: https//doi.org/ 10.1002/sia.2022

65 L. J. Xi, H. K. Wang, S. L. Yang, R. G. Ma, Z. G. Lu, C. W. Cao, K. L. Leung, J. Q. Deng, A. L. Rogach and C. Y. Chung, *J. Power Sources*, 2013, **242**, 222–229, DOI: https://doi.org/10.1016/j.jpowsour.2013.04.020.

66 F. Pawlitzek, H. Althues, B. Schumm and S. Kaskel, *Batteries*, 2017, **3**, 37, DOI: https://doi.org/10.3390/batteries3040037.

67 B. Gangaja, S. Nair and D. Santhanagopalan, *Nano-Micro Lett.*, 2020, **12**, 30, DOI: https://doi.org/10.1007/s40820-020-0366-x.

68 N. Gauthier, C. Courrèges, J. Demeaux, C. Tessier and H. Martinez, *J. Power Sources*, 2020, **448**, 227573, DOI: https://doi.org/10.1016/j.jpowsour.2019.227573.

69 Y. Ha, S. P. Harvey, G. Teeter, A. M. Colclasure, S. E. Trask, A. N. Jansen, A. Burrell and K. Park, *Energy Storage Mater.*, 2021, **38**, 581–589, DOI: https://doi.org/10.1016/j.ensm.2021.03.036.

70 H. Xia, Y. Tang, O. I. Malyi, Z. Zhu, Y. Zhang, W. Zhang, X. Ge, Y. Zeng and X. Chen, *Adv. Mater.*, 2021, **33**, 2004998, DOI: https://doi.org/10.1002/adma.202004998.

71. X. Jin, Y. Han, Z. Zhang, Y. Chen, J. Li, T. Yang, X. Wang, W. Li, X. Han, Z. Wang, X. Liu, H. Jiao, X. Ke, M. Sui, R. Cao, G. Zhang, Y. Tang, P. Yan and S. Jiao. *Adv. Mater.*, 2022, **34,** 2109356, DOI: 10.1002/adma.202109356.

72 Y. Jeon, H. K. Noh and H. K. Song, *Sci. Rep.*, 2017, **7**, 14879, DOI: https://doi.org/10.1038/s41598-017-14741-x.

73 M. Rashid and A. Gupta, *Electrochim. Acta*, 2017, **231**, 171–184, DOI: https://doi.org/10.1016/j.electacta.2017.02.040.

74 W. Guo, W. Wei, H. Zhu, Y. Hu, H. Jiang and C. Li, *eScience*, 2023, **3**, 100082, DOI: https://doi.org/10.1016/j.esci.2022.10.008.

75 H. C. Wu, Z. Z. Guo, H. P. Wen and M. H. Yang, *J. Power Sources*, 2005, **146**, 736–740, DOI: https://doi.org/10.1016/j.jpowsour.2005.03.070.

76 Ó. Vargas, Á. Caballero, J. Morales and E. Rodríguez-Castellón, *ACS Appl. Mater. Interfaces*, 2014, **6**, 3290–3298, DOI: https://doi.org/10.1021/am405197s.

77 O. Vargas, Á. Caballero and J. Morales, *Electrochim. Acta*, 2014, **130**, 551–558, DOI: https://doi.org/10.1016/j.electacta.2014.03.037.

78 Ó. Vargas, Á. Caballero and J. Morales, *Electrochim. Acta*, 2015, **165**, 365–371, DOI: https://doi.org/10.1016/j.electacta.2015.03.039.

79 L. Barbosa, F. Luna-Lama, Y. González Peña and A. Caballero, *ChemSusChem*, 2020, **13**, 838–849, DOI: https://doi.org/10.1002/cssc.201902586.

80 R. Satish, V. Aravindan, W. C. Ling, J. B. Goodenough and S. Madhavi, *Adv. Energy Mater.*, 2014, **4**, 1301715, DOI: https://doi.org/10.1002/aenm.201301715.

81 A. Varzi, D. Bresser, J. Von Zamory, F. Müller and S. Passerini, *Adv. Energy Mater.*, 2014, **4**, 1400054, DOI: https://doi.org/10.1002/aenm.201400054.

View Article Online
DOI: 10.1039/D3TA06646K

82. Y. J. Park, J. G. K, M. K. Kim, H. G. Kim, H. T. Chung and Y. Park, *J. Power Sources*, 2000, **87**, 69–77, DOI: https://doi.org/10.1016/S0378-7753(99)00362-6.